Tectonics®

RESEARCH ARTICLE
10.1029/2020TC006593

Key Points:

- Fault slip rates at the surface and extension rates at seismogenic depths were estimated at multiple sites along the Yanggao-Tianzhen Fault
- Spatial patterns in fault activity were examined along the fault
- The level of fault activity peaks at the fault center and decreases toward the fault tips

Supporting Information:

Supporting Information may be found in the online version of this article.

Correspondence to:
C. Li,
chuanyou@ies.ac.cn

Citation:
Luo, Q., Li, C., Li, X., Ren, G., & Dong, J. (2021). Slip distribution and footwall topography of the Yanggao-Tianzhen Fault (northern Shanxi Graben): Implications for the along-strike variations in fault activity and regional deformation. *Tectonics*, *40*, e2020TC006593. https://doi.org/10.1029/2020TC006593

Received 28 OCT 2020
Accepted 29 OCT 2021

Author Contributions:
Investigation: Quanxing Luo, Chuanyou Li, Xinnan Li, Guangxue Ren, Jinyuan Dong
Project Administration: Chuanyou Li
Supervision: Chuanyou Li
Writing – original draft: Quanxing Luo
Writing – review & editing: Quanxing Luo, Chuanyou Li, Xinnan Li

Slip Distribution and Footwall Topography of the Yanggao-Tianzhen Fault (Northern Shanxi Graben): Implications for the Along-Strike Variations in Fault Activity and Regional Deformation

Quanxing Luo[1,2], Chuanyou Li[1], Xinnan Li[1,3], Guangxue Ren[1], and Jinyuan Dong[1]

[1]State Key Laboratory of Earthquake Dynamics, Institute of Geology, China Earthquake Administration, Beijing, China, [2]Key Laboratory of Earth Surface Processes of Ministry of Education, Peking University, Beijing, China, [3]Earth Observatory of Singapore, Nanyang Technological University, Singapore, Singapore

Abstract Spatial patterns in fault activity were examined along the Yanggao-Tianzhen Fault (YTF) in the northern Shanxi Graben, North China. First, we reconstructed the distribution of fault slips and quantified slip rates at seven sites along the fault, based on satellite image interpretation, field investigation, topographic surveying, and optically stimulated luminescence dating. The T_3 terraces and their contemporaneous alluvial fans with a best-estimate age of 31.7 ± 1.4 kyr were used as strain markers to estimate slip magnitudes. We determined vertical slip and dip-slip rates of ~0.10–0.31 mm/yr and ~0.11–0.37 mm/yr, respectively, at the surface. Assuming fault dips of 40 ± 10° at seismogenic depths, we predicted extension rates of ~0.17–0.55 mm/yr. This suggests that at least 10% and up to 28%–54% (95% confidence interval) of the total extension of the northern Shanxi Graben is inhomogeneously partitioned by different sections of the YTF. We also evaluated the along-fault relative tectonic activity by analyzing of five widely used geomorphic indices: hypsometric integral, basin elongation ratio, asymmetric factor, valley-floor-width-to-height ratio, and mountain front sinuosity. The determined fault slip rates and geomorphic indices demonstrate that the most prominent fault activity center occurred in the middle of the fault, and that fault activity wanes toward the fault tips. Moreover, the fault activity is highly heterogeneous and fluctuates along the fault strike, which may be attributed to either fault segmentation and linkage or the possible strike-slip component of motion along the fault. Further exploration of fault kinematics and paleoseismic history is warranted.

1. Introduction

Slip rate is a fundamental component for understanding the tectonic activity of active faults (Cowie et al., 2012). Existing studies suggest that slip rates along a fault zone can vary in space and time (e.g., Bull et al., 2006; Friedrich et al., 2003; Lei et al., 2020; Rood et al., 2011; Wang et al., 2021). Often, however, the slip rate of a fault is determined by displacement and age at a given location on the fault, and the derived slip rate is then assigned to the entire fault to represent the deformation rate of the entire fault (e.g., Hu et al., 2021; Walker et al., 2021; Xiong et al., 2017). This generalization inevitably obscures the potential complexity of the along-strike variability in fault activity (Lei et al., 2021; Rood et al., 2011). Therefore, reconstructing the slip distribution and measuring slip rates at multiple sites along a fault are important. In addition, determining the slip rates of major active faults in a given region is essential for understanding contemporary deformation and assessing regional seismic hazards (Cowie & Roberts, 2001; Bai et al., 2018; Hughes et al., 2018; Rood et al., 2011). However, geological constraints on slip rates sometimes are difficult to acquire due to a lack of geomorphic markers that record fault offset or difficulties in dating the corresponding offset (e.g., faults in humid areas; Marliyani et al. [2016]). Whereas it has been well established that landscape topography encodes information on the spatial and temporal patterns and rates of tectonic deformation (Kirby & Whipple, 2012; Wobus et al., 2006). For example, active dip-slip faulting has significant control on topographic characteristics, such as elevation, slope, relief, and hydrological characteristics of the uplifted fault blocks. Quantitative analysis of these characteristics may provide insights into the long-term distribution and relative rates of deformation along a given fault (Densmore et al., 2004; Rimando & Schoenbohm, 2020; Whittaker & Walker, 2015; Yıldırım, 2014).

10.1029/2020TC006593

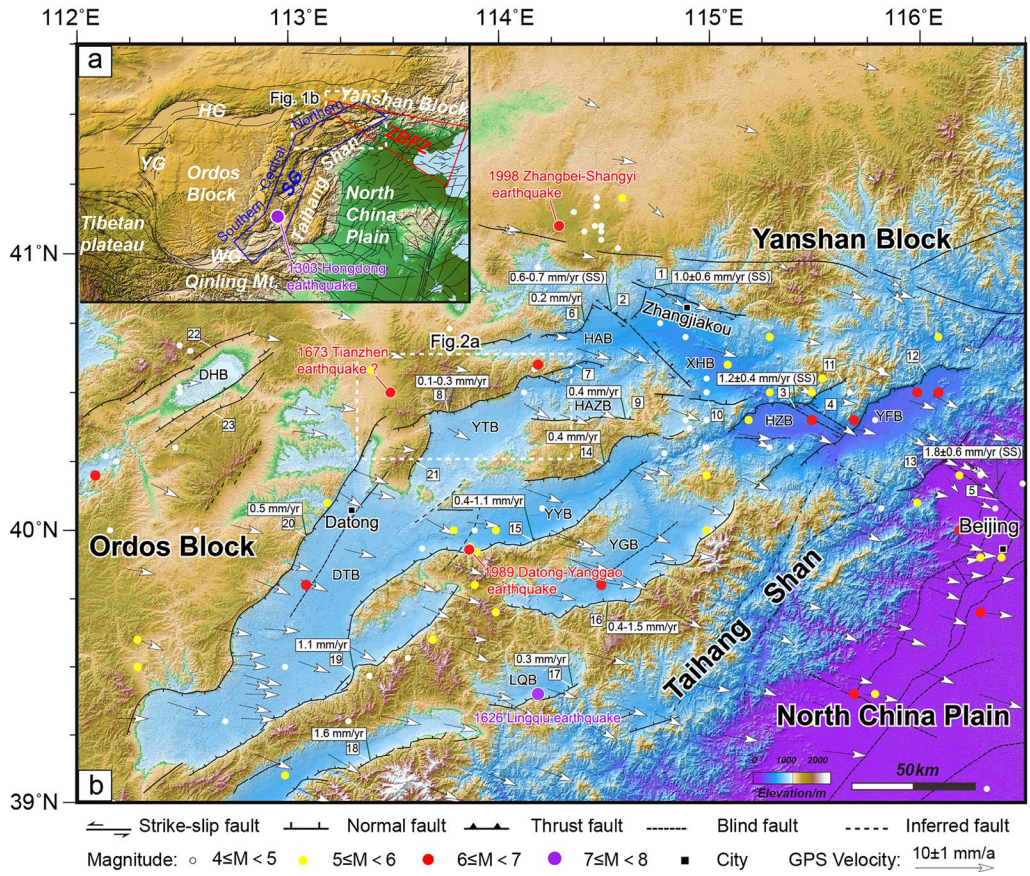

Figure 1. Tectonic setting of the study area. (a) Topographic map showing the Ordos and adjacent tectonic blocks. Black lines represent faults. Blue and red polygons represent the Shanxi Graben and the Zhangjiakou–Bohai Fault Zone, respectively. The location of the study area is outlined by the white dashed polygon. (b) Tectonic map displaying active faults in the northern Shanxi Graben, modified after Xu et al. (2016) and Middleton et al. (2017). Numbers in white boxes indicate faults with known Quaternary vertical slip rates, "SS" indicates instead a strike-slip rate. Slip rates data refer to Table S1 in the Data Set S1. Black arrows are global positioning system velocities plotted with respect to the stable Eurasian plate; data are from Zhao et al. (2017). The white dashed box shows the location of the map shown in Figure 2a. Faults: 1, Zhangjiakou Fault; 2, Ximalin Fault; 3, Xinbaoan-Shacheng Fault; 4, Huangtuyao-Tumu Fault; 5, Nankou-Sunhe Fault; 6, Huaian Basin Fault; 7, Huashan Basin Fault; 8, Yanggao-Tianzhen Fault; 9, North Xionger Shan Fault; 10, Xuanhua Basin Fault; 11, Huaizhuo Basin Fault; 12, Yanfan Basin Fault; 13, Nankou Piedmont Fault; 14, South Xionger Shan Fault; 15, Liuleng Shan Fault; 16, Yuguang Basin Fault; 17, Taibai-Weishan Fault; 18, Wutaishan Piedmont Fault; 19, Hengshan Piedmont Fault; 20, Kouquan Fault; 21, Cailiangshan East Piedmont Fault; 22, North Daihai Fault; 23, South Daihai Fault. Abbreviations: SG, Shanxi Graben; HG, Hetao Graben; YG, Yinchuan Graben; WG, Weihe Graben; DHB, Daihai Basin; DTB, Datong Basin; YTB, Yanggao-Tianzhen Basin; HAZB, Huaianzhen Basin; YYB, Yangyuan Basin; YGB, Yuguang Basin; HAB, Huaian Basin; HZB, Huaizhuo Basin; YFB, Yanfan Basin; LQB, Lingqiu Basin.

The Cenozoic grabens surrounding the stable Ordos Block in North China, are characterized by dense seismic activity and are ideal sites for investigating active extension and continental rift evolution (Figure 1a; Middleton et al., 2016; Rao et al., 2014, 2020; State Seismological Bureau, 1988). Among these graben systems, the Shanxi Graben (SG) formed most recently, likely in the early Pliocene (Figure 1a) (Xu et al., 1993), and was responsible for the 1,303 Mw 7.2–7.6 Hongdong earthquake in its central domain, which had a death toll of approximately 270,000 (Xu et al., 2018; State Seismological Bureau, 1988). While no historical M 7+ earthquakes have been documented in the northern domain of SG (Figure 1b; Xu et al., 2002), it is worth noting that the northern SG is within a few dozen kilometers of Beijing (Figure 1b). As a result, the late Quaternary activity of faults in this region requires further study.

The Yanggao-Tianzhen Fault (YTF) is an active normal fault in the northern SG (Figure 1b; Duan, 1994; Xu et al., 2002). While the YTF may have produced an estimated M 6.5 event in 1673 (Gu et al., 1983; Lee

et al., 1976; Li et al., 2007; Middleton et al., 2017; Wan et al., 2006), its slip rate has not yet been precisely determined. Offsets of geomorphic markers such as alluvial fans and terraces have been documented in some sites along the fault, yet the resolution of slip rate calculations has been limited by older dating methods. For example, Xu et al. (2002) estimated a vertical slip rate of ~0.34 mm/yr based on topographic surveying and an inferred age, and Duan (1994) determined a vertical slip rate of ~0.13 mm/yr over the late Pleistocene using thermoluminescence (TL) dating. However, these previous study sites are concentrated along a small part of the YTF (Figure 2b), which limits our understanding of the along-strike variations in fault activity and its role in accommodating regional deformation.

In this study, we reconstructed the slip distribution and quantified fault slip rates along the YTF over the late Quaternary. This was done using interpretations of high-resolution satellite imagery, and digital elevation models derived from unmanned-aerial-vehicle (UAV) structure-from-motion (SfM) photogrammetry, geomorphic mapping, and optically stimulated luminescence dating. We then compared the slip history at seven sites using isochronous markers, to identify spatial patterns in fault activity and understand the tectonic role the YTF has played in the northern SG. To better characterize the spatial pattern of fault activity, we also analyzed the features of footwall topography and measured five widely used geomorphic indices to evaluate relative tectonic activity: hypsometric integral, basin elongation ratio, asymmetric factor, valley-floor-width-to-height ratio, and mountain front sinuosity. Finally, we synthesized our results to understand the spatial pattern of fault activities and discuss potential seismic hazards.

2. Tectonic Settings

The graben systems around the Ordos Block are major late Cenozoic extensional features in North China (Figure 1a;Zhang et al., 1998). The Pliocene-Quaternary SG is situated to the east of the Ordos Block and west of the Taihang Shan and can be geometrically divided into northern, central, and southern domains (Figure 1a). Our study focused on the northern domain, which is a typical basin-and-range province characterized by a series of ENE-trending normal fault-controlled basins separated by uplifted mountain ranges (Figure 1b). Geological, GPS, and seismicity studies have shown that the northern SG is extending along a NNW-SSE strike at 1–2 mm/yr (Middleton et al., 2017; Shi et al., 2015; Zhao et al., 2017; Zhang et al., 1998, 2009, Y. Q. Zhang et al., 2003). In addition, our study area is also the locus of two main tectonic belts that intersect in North China; the NE-trending dextrally transtensional SG, and the NW-trending left-lateral strike-slip Zhangjiakou-Bohai Fault Zone (ZBFZ; Figure 1a; Xu et al., 1998; Xu et al., 2002; Zhang et al., 2009). The ZBFZ delineates the boundary between the North China Plain in the south and the Yanshan Block in the north (Xu et al., 1998; P. Z. Zhang et al., 2003; Zhang et al., 2018). It has a left-lateral slip rate of approximately 2 mm/yr based on GPS observations (Wang & Shen, 2020).

Our study area has three sets of active faults, with strikes of ENE, NNE, and NW (Figure 1b). The ENE-trending group consists of the primary structures in the northern SG, including the Huaian Basin Fault, YTF, North Xionger Shan Fault, South Xionger Shan Fault, Liuleng Shan Fault, Yuguang Basin Fault, Taibai-Weishan Fault, Huaizhuo Basin Fault, and Yanfan Basin Fault. According to previous studies (e.g., Deng et al., 1994; Fang et al., 1994; Middleton et al., 2017; Shen & Wang, 1994; Sun, 2018; Xu et al., 2002; Wang, 2012, etc.), the vertical slip rates of these normal faults vary from 0.1 to 1.5 mm/yr (Figure 1b). The NNE-trending fault zone includes the Kouquan Fault, Hengshan Piedmont Fault, and the Cailiangshan East Piedmont Fault. The Kouquan Fault is dominated by normal faulting but may have a dextral strike-slip component with vertical slip rates of 0.2–0.5 mm/yr (Ding & Lu, 1983; Li et al., 2013; Xu et al., 2011). The NW-trending faults in the study area include the Zhangjiakou Fault, Ximalin Fault, and other blind faults in the Huaizhuo and Yanfan basins; they are characterized by left-lateral strike-slip movement. Previous studies on the slip rates of these three fault sets are summarized in Table S1 in Data Set S1. Published data have also shown that the majority of the faults bounding the basins in the northern SG are Holocene active faults (Xu et al., 2002, 2017). However, seismicity in the northern SG is primarily characterized by moderate earthquakes both in historical and instrumental records, and there is only one reported event with an estimated magnitude of ~M 7 (1626 Lingqiu Earthquake; Figure 1b; Shen & Wang, 1994; Xu et al., 2002). The most recent events resulting in casualties and severe damage in the northern SG are the Datong-Yanggao Ms 6.1 earthquake (October 1989) and the Zhangbei-Shangyi Ms 6.2 earthquake (January 1998; Figure 1b).

10.1029/2020TC006593

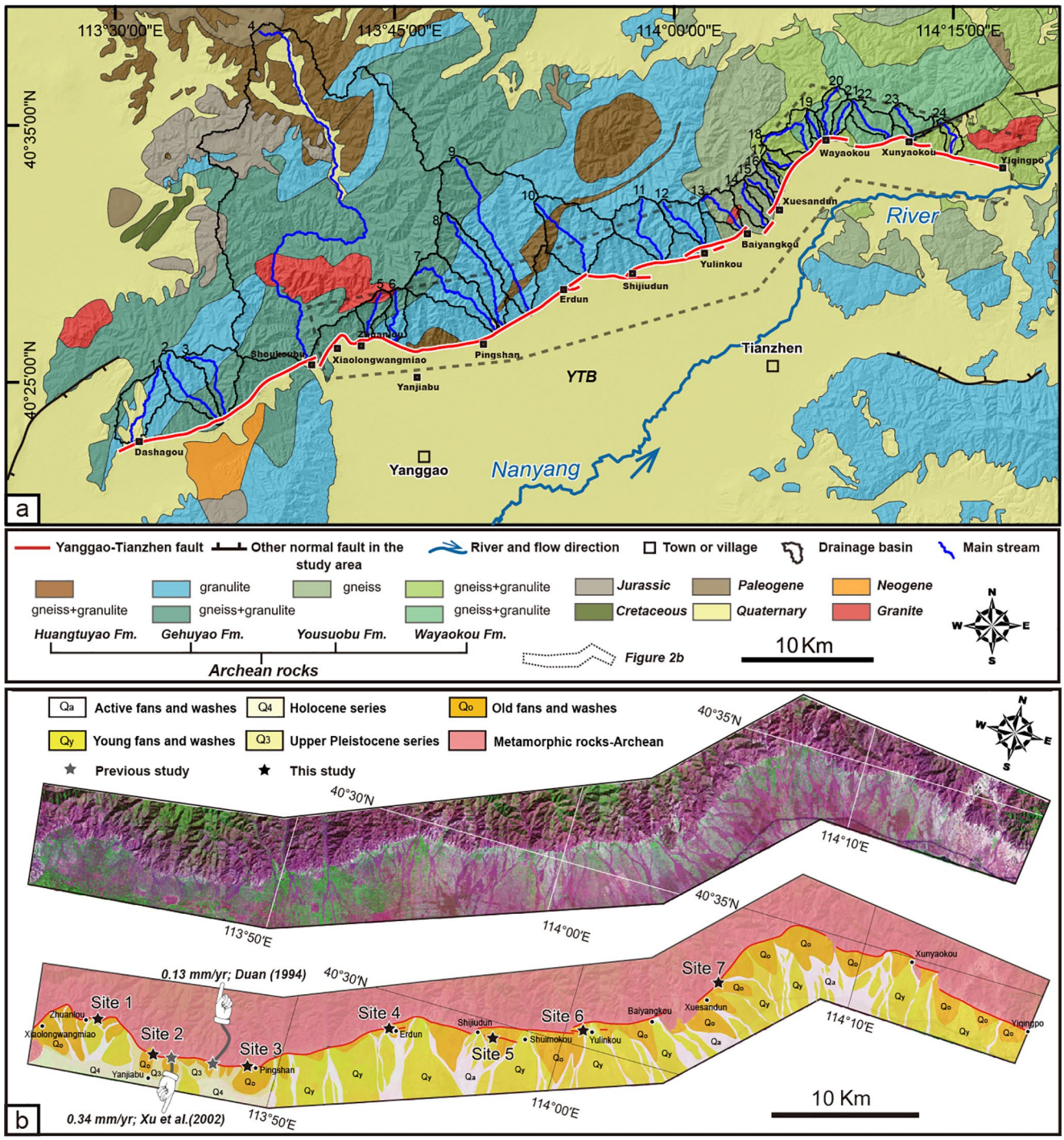

Figure 2. (a) Geological map of the YTF referenced to the 1:200,000 geological database (Li et al., 2017). (b) Landsat satellite image and geomorphic map of the YTF, showing the distribution of the fault scarp, multi-stage alluvial fans.

The YTF is an active normal fault that extends approximately 75 km from Dashagou, Fengzhen, Inner Mongolia (113.504°E, 40.362°N) in the west, to Yiqingpo, Tianzhen, Shanxi (114.288°E, 40.537°N) in the east (Figure 2a; Luo et al., 2020). It defines the northern boundary of the Yanggao-Tianzhen Basin (YTB), east of Xiaolongwangmiao village (Figure 2b; Duan, 1994; Xu et al., 2002). The overall strike of the YTF changes from ENE in the west to NE in the vicinity of Baiyangkou village, and then to WNW at Wayaokou village in the east (Figure 2a). The WNW-trending segment is characterized by oblique-normal movement with a

minor sinistral component, whereas the ENE- and NE-trending segments are dominated by normal faulting (Luo et al., 2020). The fault trace east of Xiaolongwangmiao village (Figure 2a) is ~58 km long and consists of two major Holocene active segments separated by a right stepover in the vicinity of Baiyangkou village. The segment west of Xiaolongwangmiao is a late-Pleistocene-active fault (Figure 2a; Luo et al., 2020; Xu et al., 2002). The YTB is an asymmetrical basin, and the basin depth increases from south to north, whereas the width decreases from west to east (Figure 2a). Sediments in the YTB range from 200 to 500 m in thickness over the metamorphic basement (Zheng et al., 2000). Xu and Ma (1992) suggested that extension in the YTB started in the middle-late Pliocene. The bedrock range on the footwall block primarily consists of Precambrian metamorphic rocks (Figure 2a).

3. Methods

3.1. Topographic Data Acquisition: UAV Photogrammetry

High-resolution digital elevation data have been used extensively in studies on active tectonics (e.g., Angster et al., 2016; Ren et al., 2016; Zielke et al., 2010). To better illustrate the details at specific sites and acquire the displacement of the deformed geomorphic surfaces, we created high-resolution digital elevation models (DEMs) (<0.5 m/pix) using UAV photogrammetry (e.g., Johnson et al., 2014; Lucieer et al., 2014; Westoby et al., 2012). At Sites 1, 3, and 6 (Figure 2b), before acquiring photographs, ground control point (GCP) targets were fixed through the targeted areas and surveyed using a Trimble Geo7X post-processed kinematic (PPK) differential global positioning system (DGPS) with a horizontal precision of 3 mm +1 ppm RMS, and a vertical precision of 3.5 mm +0.5 ppm RMS. The surveyed GCPs were then used to calibrate the derived DEMs in the Agisoft Photoscan software. At Sites 2, 4, 5, and 7 (Figure 2b), the photographs used to process high-resolution DEMs were collected by a low-flying DJI Phantom 4 UAV equipped with a Network Real-Time Kinematic (NRTK) module, which allowed a real-time differential between the aircraft and the local GNSS system. The NRTK positioning technology can achieve centimeter-level positioning accuracy without the need for the ground control points generally required in traditional SfM surveys (https://www.dji.com/phantom-4-rtk?site). DJI Phantom 4 RTK UAVs have been used in other recent active tectonics studies to generate high-resolution DEM data (e.g., Liang et al., 2019). Using high-resolution SfM-derived DEMs, hillshade images and contour maps were created in ArcMap and Surfer for geomorphic mapping and further analysis at each study site. At Site 4, we photographed an outcrop to reconstruct the surface based on UAV photogrammetry (e.g., Bemis et al., 2014; Wilkinson et al., 2016). A high-resolution ortho-photomosaic was then generated for the identification of strata and structures in the fault zone and to measure the displacement of the strata (Figure S4a in Data Set S1).

3.2. Dating of Deformed Geomorphic Markers

Application of ^{14}C dating to the geomorphic surfaces in our study area was difficult because of the general lack of organic materials. The terrestrial cosmogenic nuclide (TCN) surface exposure dating technique was also not employed because the majority of the alluvial fan treads have been modified by human agricultural activities. In addition, some of the alluvial fans were covered by thick loess (>2 m), which complicated the dating of displaced geomorphic surfaces using the TCN surface exposure dating method, although the shielding effect of loess cover could be corrected (Hetzel et al., 2004). Field observations identified silt and fine sand layers in the gravels of terraces (Figures 6c, 7e, and 10f) and eolian loess covering the surface (Figures 7e, 8e, 9c, and 10f). Therefore, we used the optically stimulated luminescence (OSL) dating method to constrain the abandonment ages of displaced alluvial fans and terraces and further quantify fault slip rates. Our sampling strategy relied on the assumption that the upper sedimentary layer in the vicinity of a terrace or alluvial fan surface provided the maximum abandonment age of the geomorphic surface, which could be used to estimate the minimum slip rate of the fault. The base of the eolian loess that covered the fan or terrace surface should be slightly younger than the surface, and provide a minimum abandonment age of the surface (Hu et al., 2021; Wu et al., 2019). In total, five OSL samples were collected, one of which (OSL-YTF-21) was collected from the bottom of the eolian loess layer covering the terrace. Four samples (OSL-TZF-01, OSL-YTF-19, 20, 23) were collected from the silt or fine sand layer beneath the alluvial fan or terrace surface. The OSL samples were collected using stainless steel tubes (20 cm long and 5 cm diameter) from approximately 30 cm below the surface. This was done to avoid disturbances related to surficial processes

Table 1
OSL Dating Results

Sample code	Latitude (°N)	Longitude (°E)	Elevation (m)	Depth (m)	Protocol	U (ppm)	Th (ppm)	K (%)	Water content (%)	De (Gy)	Dose rate (Gy/kyr)	Age[a] (kyr)
OSL-TZF-01[b]	40.4285	113.8116	1130	0.40	SMAR	1.09 ± 0.32	5.36 ± 0.08	0.97 ± 0.02	11	59.7 ± 3.6	2.0 ± 0.1	29.7 ± 2.5
OSL-YTF-19[c]	40.4284	113.8116	1127	2.50	SMAR	2.63 ± 0.63	5.79 ± 0.22	1.42 ± 0.06	15.66	73.7 ± 3.5	2.3 ± 0.2	31.8 ± 3.6
OSL-YTF-20[c]	40.4617	113.8908	1120	3.20	SMAR	1.20 ± 0.63	5.69 ± 0.23	1.44 ± 0.06	5.97	85.3 ± 5.7	2.5 ± 0.3	34.4 ± 4.6
OSL-YTF-21[c]	40.4617	113.8909	1122	2.10	SMAR	2.85 ± 0.73	9.52 ± 0.32	1.54 ± 0.06	3.09	95.5 ± 3.6	3.5 ± 0.4	27.6 ± 3.5
OSL-YTF-23[c]	40.5199	114.0887	1170	1.40	SAR	2.42 ± 0.96	9.01 ± 0.29	1.94 ± 0.08	3.74	78.9 ± 4.7	3.0 ± 0.2	26.3 ± 2.6

[a]The age uncertainty is 2 sigma. [b]Sample measured in the State Key Laboratory of Earthquake Dynamics, Institute of Geology, China Earthquake Administration. [c]Samples measured in the Key Laboratory of Crustal Dynamics, China Earthquake Administration.

and to ensure that samples were taken from the original sedimentary layers. The tubes were hammered into the sediment, filled, and then both ends were immediately sealed with aluminum foil and taped to prevent light leakage and loss of water during transport and storage. The OSL samples were measured at the Key Laboratory of Crustal Dynamics, China Earthquake Administration (CEA), and the State Key Laboratory of Earthquake Dynamics, Institute of Geology, CEA. The OSL ages were calculated using the mean equivalent dose values for each sample. The detailed preparation and experimental procedures are provided in Text S1 in Data Set S1. The OSL dating results are listed in Table 1.

3.3. Offset Measurement and Slip Rate Calculation

High-resolution UAV-acquired DEMs were used to quantitively measure the magnitude of deformation for the displaced geomorphic markers, by extracting topographic profiles perpendicular to the fault scarps in 3D visualization software such as Quick Terrain Modeler or Global Mapper. We used the approach developed by Thompson et al. (2002) for the vertical separation and dip-slip offset calculations (Figure 3a). The least-squares linear regression method was used to fit points and determine the gradient and the intercept of lines representing the hanging wall ($y_h = m_h x + b_h$), footwall ($y_f = m_f x + b_f$) and scarp ($y_s = m_s x + b_s$; Figure 3a). The mean and standard deviation of the slope and intercept of the fitted lines were also calculated using this line-fitting process. The vertical separation and dip-slip offset of a normal fault are given by the following equations:

$$v(x) = x(m_f - m_h) + b_f - b_h, \tag{1}$$

and

$$s = \frac{x(m_s - m_h) + b_s - b_h}{\sin\delta - m_h \cos\delta} + \frac{x(m_f - m_s) + b_f - b_s}{\sin\delta - m_f \cos\delta}, \tag{2}$$

where v is the vertical separation, s is the fault dip-slip offset, x is the horizontal distance along the profile, and δ is the fault dip angle from field measurements on the exposed fault planes. The average fault slip rate (u) was calculated by dividing the fault displacement (s) by the age of the offset landform (t):

$$u = \frac{s}{t} \tag{3}$$

The calculation of the horizontal extension rate is explained in detail in Section 5.1.

Following the approach of Hughes et al. (2018), Rood et al. (2011), Thompson et al. (2002), and Wei et al. (2020), we calculated slip rates, scarp heights, and dip-slip offsets and their uncertainties, by applying Monte Carlo simulations that allowed for the incorporation of uncertainty estimates for a large number of parameters of interest. For example, input variables used in Monte Carlo simulations to calculate slip rates were surface age, fault position along the scarp, fault dip, geomorphic slopes, and intercepts (Figure 3b).

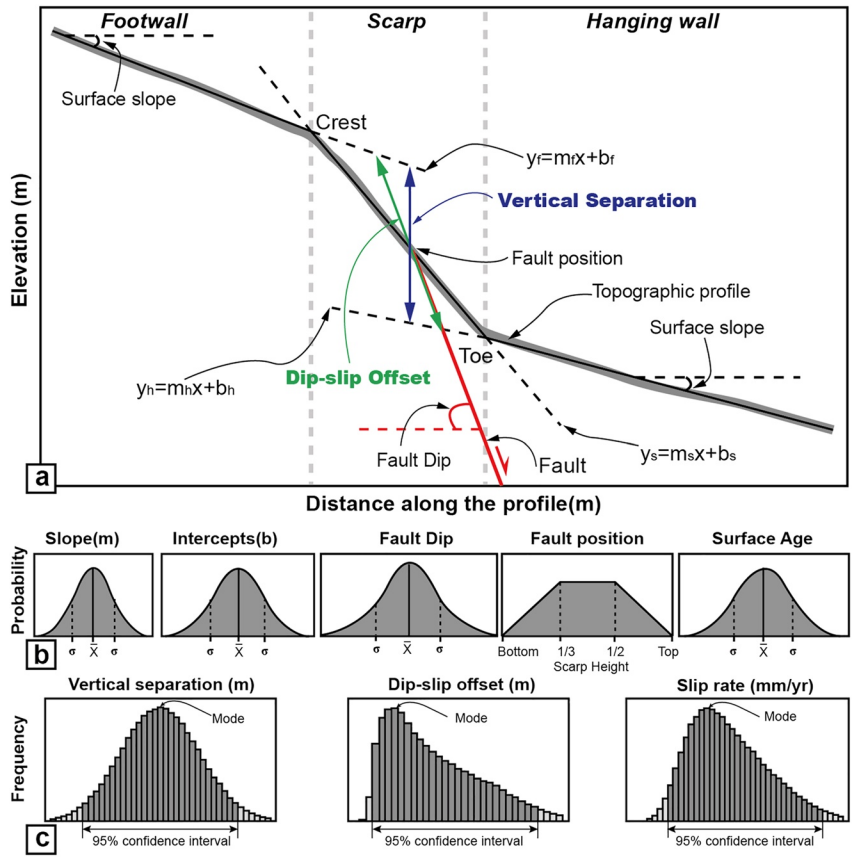

Figure 3. Method for estimating fault displacement across a fault scarp. (a) Schematic map showing parameters and equations used to calculate fault displacement and slip rates across a normal fault scarp. (b) The PDFs of five inputs combined in a Monte Carlo simulation to provide the best estimate of magnitude and rate of fault slip. (c) Histograms showing the results of Monte Carlo simulations.

In the Monte Carlo simulations, each input parameter was assigned a best-fit probability density function (PDF). We assigned a Gaussian distribution (also called a normal distribution, defined by the mean and standard deviation) for slope, intercept, fault dip, and surface age. We observed exposed fault planes at each of the seven sites in this study. Therefore, the dip-slip offset and slip rate was calculated based on the dip angle measurements at each locality. The measurement uncertainties were defined as ±3° towing to the change in fault dips on the outcrop scale. Finally, we modeled the fault position within the scarp using a trapezoidal PDF, which assumed that the fault position was most likely between one-half and one-third of the scarp height, measured from the base of the scarp with the likelihood decreasing to zero at the top and base of the scarp (Hughes et al., 2018; Rood et al., 2011). In each calculation, all of the input parameters were randomly sampled based on the assigned PDF over 500,000 or 1,000,000 trial runs. Histograms showing the frequency of predicted values were used to define the mode and 95% confidence interval for each output parameter of interest, for example, vertical separation, dip-slip offset, and slip rate (Figure 3c). In locations where multiple parallel fault strands cut a single geomorphic surface (e.g., Sites 4 and 5), an additional Monte Carlo simulation was used to sum individual offsets using the total slip histogram for each strand as an input. All Monte Carlo simulations were performed using Oracle Crystal Ball, a spreadsheet software package for risk analysis (https://www.oracle.com/middleware/technologies/crystalball.html).

3.4. Geomorphic Analysis

Because of the widespread availability of high-quality DEMs and geographic information system (GIS) software, the analysis of geomorphic indices has been an important method for evaluating the relative tectonic activity along fault zones (Cheng et al., 2018; Hamdouni et al., 2008; Ntokos et al., 2016; Rimando & Schoen-

bohm, 2020; Yıldırım, 2014). To better depict the along-strike variations in fault activity, we carried out a geomorphic analysis on the footwall block of the YTF, based on the 30 m-resolution ASTER GDEM (V2). Although there are some issues with the quality of the ASTER GDEM V2 data set (Boulton & Stokes, 2018), its vertical and horizontal accuracy have been shown to be sufficient for measurements aimed at describing regional trends in relative tectonic activity (e.g., Rimando & Schoenbohm, 2020). Using the Hydrology tools in ArcGIS, a total of 24 drainage basins were extracted (No. 1–24 from west to east; Figure 2a). These drainage basins all rise from the topographic ridge of the range, and their outlets are all located near the trace of the fault. As shown in Table S6 in Data Set S1, there was a wide range in the area of these drainage basins from 1.62 to 289.34 km^2 (No.19 and 4, respectively). Basin No. 4 was the largest and, based on its regional extent, should be antecedent to the YTF. With the exception of basin No. 4, we believe that all the other basins developed in response to the displacement of the fault. Therefore, we excluded basin No. 4 from further analysis. Thus, basin No.9 (53.20 km^2) was the largest analyzed drainage basin, with all basins greater than the threshold value (1 km^2). Previous studies have shown that basins smaller than this critical threshold value may be dominated by non-fluvial processes (Montgomery & Foufoula-Georgiou, 1993; Wobus et al., 2006) and may be too young to yield reliable morphometric measurements (Bull & McFadden, 1977; Rimando & Schoenbohm, 2020). Basic morphometric parameters such as area (A), mean elevation (H_{mean}), maximum elevation (H_{max}), minimum elevation (H_{min}), and the length of the main stream of each drainage basin (L_s), were then acquired for each basin. Based on these parameters, we evaluated relative tectonic activity by measuring five widely used geomorphic indices: hypsometric integral (HI), basin elongation ratio (R_e), asymmetric factor (A_f), valley-floor-width-to-height ratio (V_f), and mountain front sinuosity (S_{mf}). These indices have been shown to correlate with tectonic activity, and details of these parameters are illustrated in Text S2 in Data Set S1 (Bull & McFadden, 1977; Cox, 1994; Pike & Wilson, 1971; Schumm, 1956; Strahler, 1952). As the footwall range was composed almost exclusively of Archean gneiss and granulite (Figure 2a), lithology should not be a significant control on differences in basin size, relief, and geomorphic indices. In addition, we also assumed the analyzed drainage basins had a uniform climate and base-level history.

The classification of tectonic activity based on measured geomorphic indices is a common practice in geomorphic parameter studies. For example, several studies use a combination of two indexes, S_{mf} and V_f, to provide semi-quantitative information on the relative degree of tectonic activity of mountain fronts (Bull & McFadden, 1977; Rockwell et al., 1984; Silva et al., 2003). However, this method assigns a tectonic activity class to an individual mountain front and does not reveal any information about along-strike variations in tectonic activity along the mountain front. Alternatively, Hamdouni et al. (2008) proposed another index, Iat, to represent the relative tectonic activity. Iat is a combined index that can involve multiple indices and assess relative tectonic activity, not only along a particular mountain front but also over an area. To acquire the Iat index, we first divided each index into three classes: class 1, high activity; class 2, moderate activity; and class 3, low activity. The specific criteria for the divisions are shown in Table S4 in Data Set S1 and Figure 13. Subsequently, by averaging the different classes of geomorphic indices, we obtained the values of S/n, where S is the sum of the classes of all geomorphic indices of each basin, and n is the number of types of geomorphic indices. In this study, $n = 5$, because five different geomorphic indices were used. Finally, the S/n was divided into four classes, where class 1 had very high tectonic activity with values of S/n between 1 and 1.5 (Iat = 1), class 2 had high tectonic activity with values of $S/n > 1.5$ but <2 (Iat = 2), class 3 had moderately active tectonics with $S/n > 2$ but <2.5 (Iat = 3), and class 4 had low active tectonics with values of $S/n > 2.5$ (Iat = 4). Herein, we simplified the method of Hamdouni et al. (2008) and followed the example of Cheng et al. (2018), whose values of Iat were simply given by the equation Iat = S/n. Thus, Iat is inversely proportional to the tectonic activity (i.e., slip rate; Cheng et al., 2018; Hamdouni et al., 2008). The results of the geomorphic analysis are summarized in Table S6 in Data Set S1.

4. Results

4.1. Site Descriptions, Sample Age, and Fault Offsets

In this study, we used remote sensing and field investigations to identify fault traces and deformed geomorphic surfaces. Fault outcrops and tectonic landforms, such as linear fault scarps, were used to confirm the fault location. Based on a Landsat satellite image, the alluvial fans in the YTB were divided into two

main stages according to the degree of surface incision and dissection as well as their relative geometrical relationships (Figure 2b). The older and younger fans were labeled as Q_o and Q_y, respectively (Q_o is the old fans and washes, Q_y is the young fans and washes). Compared to the younger fans (Q_y), the older fans (Q_o), were a lighter color in the image, severely cut by gullies, and did not extend a significant distance from the mountain front (Figure 2b). Alluvial fans and fluvial terraces were mapped across the YTF in more detail at seven sites based on the SfM-derived DEMs and field investigations. Topographical profiles were also built to determine the fault offsets across the fault scarps. We collected OSL dating samples at locations where geochronology samples were available, to constrain the age of the geomorphic surfaces and further estimate the slip rates.

4.1.1. Site 1: T_3

Site 1 is located to the east of Zhuanlou village (Figure 2b). Four fluvial terraces (labeled T_1 to T_4 from lowest to highest or from youngest to oldest) are preserved on the northern side of the fault along the flanks of stream channel SC-1 (Figure 4a). Field observations show that terraces T_2–T_4 were displaced by the YTF (Figures 4b and 4c). The minimum vertical separation of T_4 was 11.1 + 0.7/-1.0 m, as T_4 was not preserved on the southern side of the fault trace (Figure 4a and Figure S1a in Data Set S1). The vertical separation of the T_2 terrace was 2.5 ± 0.3 m (Figure 4a and Figure S1b in Data Set S1). Two topographic profiles across the fault scarp on the T_3 terrace at the east bank of the SC-1 had vertical separations of 2.4 + 0.5/−0.3 m and 3.1 ± 0.2 m. According to a measurement of fault dip (50 ± 3°) by Luo et al. (2020), the corresponding fault dip-slips of these two topographic profiles were 2.8 + 0.5/−0.6 and 3.3 + 0.4/−0.3 m, respectively (Figure 4a and Figures S1c and S1d in Data Set S1).

4.1.2. Site 2: Q_o

At Site 2 (Figure 2b), north of Yanjiabu village, we identified a group of fault scarps on the older alluvial fans (Q_o) using a Google Earth image captured in 2012 (Figure 5a). However, the records of Quaternary faulting were poorly preserved. Fault scarps on the west side of stream channel SC-2 were modified during the construction of a solar power station, so only the fault scarps east of the stream channel SC-2 were observed during our field visit (Figures 5b and 5d). A topographic profile of the scarp in the fan surface gave a vertical separation of 6.5 + 0.6/−0.3 m and a total slip estimate of 6.8 + 0.7/−0.5 m when integrated with a fault dip of ~68 ± 3° (Figures 5c and 5d).

4.1.3. Site 3: Q_o

Site three is west of Pingshan village (Figure 2b). At this site, the contour map showed some slightly curved, approximately EW-trending fault scarps cutting through the Q_o alluvial fans (Figure 6a). Two OSL samples (OSL-TZF-01 and OSL-YTF-19) were collected from alluvial fan deposits exposed on the east wall of stream channel SC-3. These two samples were from silt layers approximately 0.4 and 2.5 m below the fan surface and yielded ages of 29.7 ± 2.5 and 31.8 ± 3.6 kyr, respectively (Figures 6b–6e). The actual abandonment age of the fan should be younger than 29.7 ± 2.5 kyr. Two topographic profiles over 250 m and normal to the fault scarp were extracted. These profiles gave vertical separations of 5.4 + 0.2/-0.1 and 5.5 + 0.5/−0.4 m (Figure 6a and Figure S2 in Data Set S1). Incorporating a fault dip of 65 ± 3° measured in the field, resulted in total dip-slips of 5.7 + 0.4/−0.2, and 5.8 + 0.6/−0.4 m, respectively (Figure 6b and Figure S2 in Data Set S1).

4.1.4. Site 4: T_3

West of the Erdun village (Figure 2b), three stages of fluvial terraces (T_1–T_3) developed along stream channel SC-5 (Figures 7a and 7b). Among these, the T_3 and T_2 terraces were displaced by the YTF, leaving several stepped fault scarps. The scarps were mapped in detail by combining field investigations with the surveyed DEMs (Figures 7a and 7b). The pictures were taken in the field clearly showed features of fault scarps and outcrops (Figures 7c and 7d; Figure S4 in Data Set S1). We identified two and three groups of scarps east and west of SC-4 on the T_3 terrace, respectively. Topographic profiles across the fault scarps on the T_3 terrace yielded vertical separations of 8.2 + 0.6/−0.4, and 9.8 + 0.4/−0.3 m, and cumulative dip-slip magnitudes of 9.9 + 0.9/−0.7, and 11.8 + 0.8/−0.7, respectively, when combined with a field-measured of dip of 54 ± 3° (Figure 7b and Figure S3 in Data Set S1).

10.1029/2020TC006593

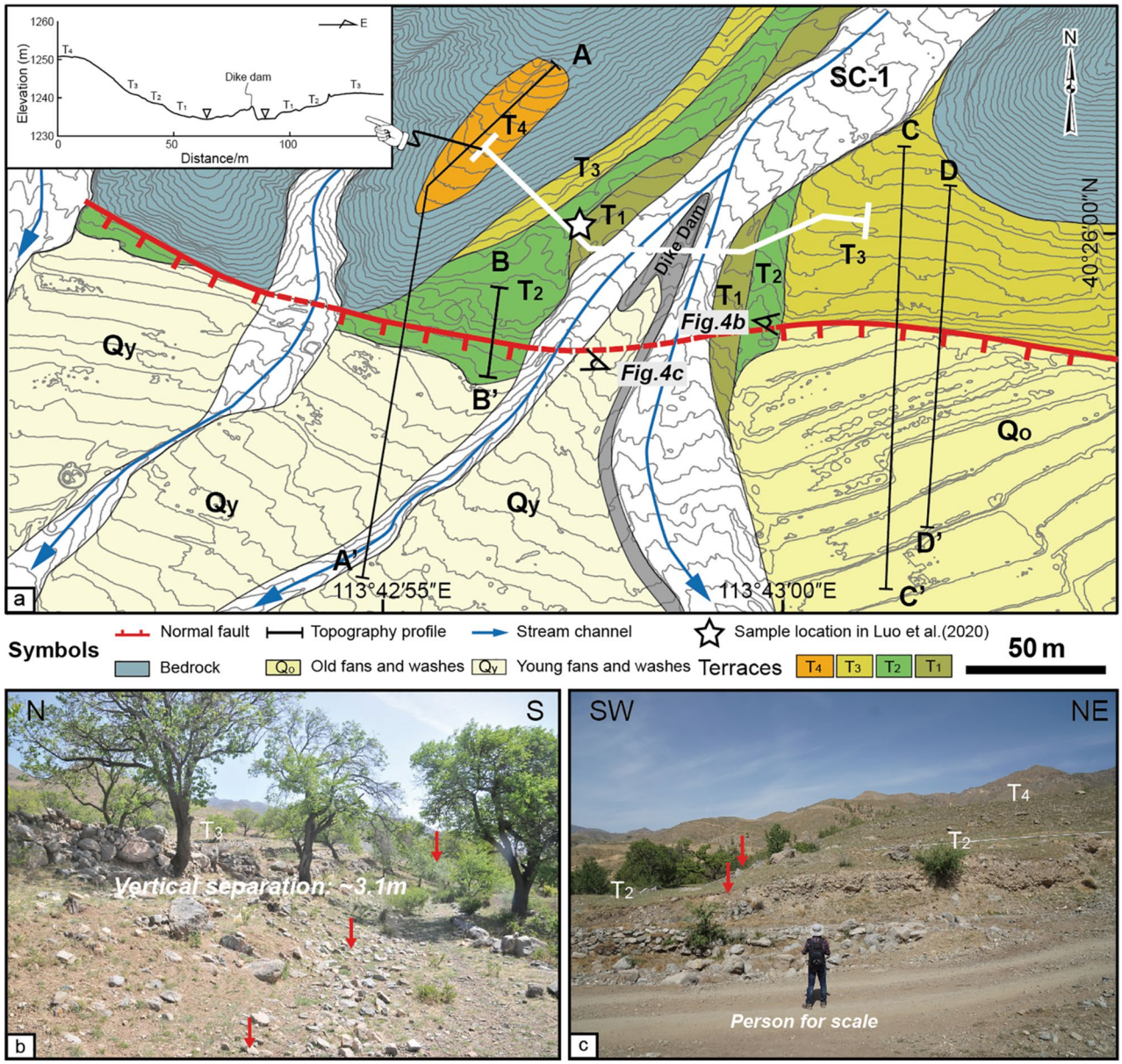

Figure 4. Displaced geomorphic features along the fault trace at Site 1. (a) Quaternary map showing active fault trace and offset geomorphic surfaces. The topographic contour interval is 1 m. The inset panel displays a topographical profile along the thick white line, showing the terrace staircases. (b) and (c) Field photos of the displaced geomorphic features. Arrows in red indicate the fault location. The perspective of each photo is shown in Figure 4a.

Figure 7e shows a sketch map of the fault zones exposed on the west wall of SC-4. The thick, horizontally stratified alluvium is blanketed with a locally variable loess cover typically >2 m in thickness. The vertical separation of the loess–gravel contact across the fault zones is ~9.4 m, with an estimated ±1.0 m of uncertainty due to the choice of piercing lines in the contact. This vertical separation corresponds to a dip-slip offset of 11.7 ± 2.6 m (using a dip of 54 ± 3°), which is comparable to the dip-slip offsets indicated by the fault scarps on the T_3 terrace surface. Two OSL samples were collected and tested to determine the timing of the abandonment of the T_3 terrace. OSL-YTF-20 was taken from a silt interlayer ~1 m below the loess–gravel contact, and OSL-YTF-21 was sampled from the bottom of the loess layer approximately 0.2 m above the loess–gravel contact. They yielded ages of 34.4 ± 4.6 and 27.6 ± 3.5 kyr, respectively (Figures 7f–7i). Thus, the abandonment of the T_3 terrace should be between these two ages.

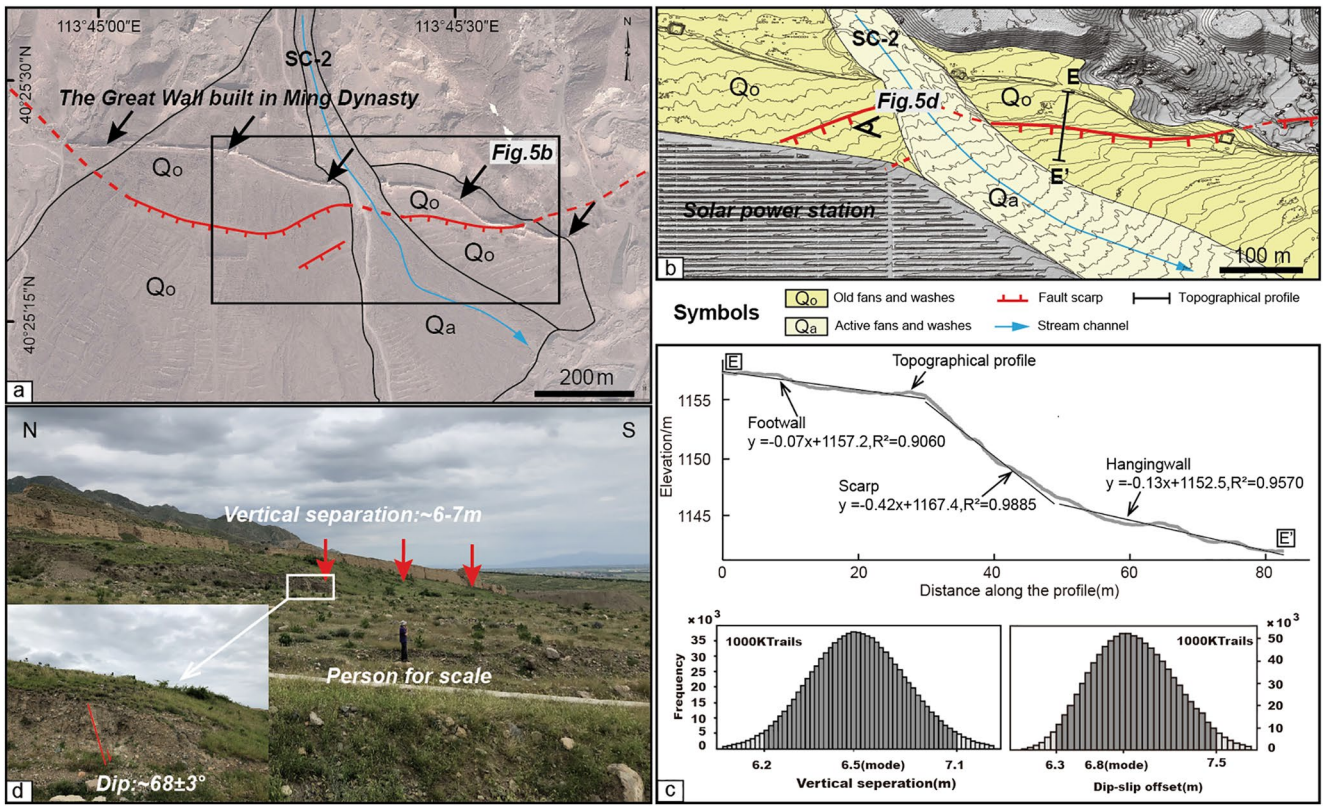

Figure 5. Displaced geomorphic features along the fault trace at Site 2. (a) Google Earth image showing fault scarps on the older fans (Q_o). The arrows in black indicate the location of the Great Wall. The black rectangular box outlines the area of Figure 5b. (b) Hillshade map showing the fault trace and the location of the topographic profile. The topographic contour interval is 2 m. (c) Topographic profile of E-E' and corresponding frequency histograms during Monte Carlo simulations. (d) Field photo of the deformed alluvial fan and fault outcrop. The perspective of this photo is shown in Figure 5b. The red arrows indicate the fault location.

4.1.5. Site 5: Q_o

Based on an analysis of Google Earth imagery and field observations, two stages of alluvial fans were identified at Site 5, between the Shijiudun and Shuimokou village (Figures 2b and 8). The older alluvial fans (Q_o) were heavily dissected by gullies and were cut by two groups of continuous fault scarps running EW. However, no clear fault scarps could be observed in the younger fans (Q_y) (Figures 8a and 8d). The surfaces of the fans have been partly altered by farming activities, forming many anthropogenic scarps. A small-scale fault outcrop was found along the linear fault scarps, enabling us to differentiate fault scarps from anthropogenic scarps (Figures 8c and 8e). Figure 8e also shows a sedimentary sequence with a gravel layer below and a loess layer above, which is similar to the sedimentary structure of the T_3 terrace at Site 4. We conducted a UAV survey, and three topographic profiles were built across two fault scarps offsetting the older fan (Q_o). This yielded summed vertical separations of 7.2 + 1.0/−1.1, 4.4 + 0.6/-0.8, and 4.4 ± 1.2 m and total dip-slip offsets of 7.4 + 1.0/−1.2, 4.4 ± 0.7, and 4.4 + 1.3/−1.2 m, respectively, based on the 73 ± 3° fault dip of the exposed fault plane (Figure 8c and Figure S5 in Data Set S1).

4.1.6. Site 6: Q_o

At Site 6 (Figure 2b), between Yulinkou village and Huapimiao village, two stages of alluvial fans were well-preserved (Figure 9). The older alluvial fans (Q_o) were dissected by densely developed gullies, and the surfaces of the younger alluvial fans (Q_o) were smoother. Several fault outcrops in the field indicated that the fault zone comprises two subparallel branches (Figure S6 in Data Set S1). One branch lies along the apexes of the alluvial fans, forming a linear contact between the bedrock mountain range and the basin. The other branch is located in the basin and is evidenced by fault scarps on the older alluvial fans (Figure 9b). Toward west of Yulinkou village, a fault profile at the edge of the alluvial fan revealed that the alluvium

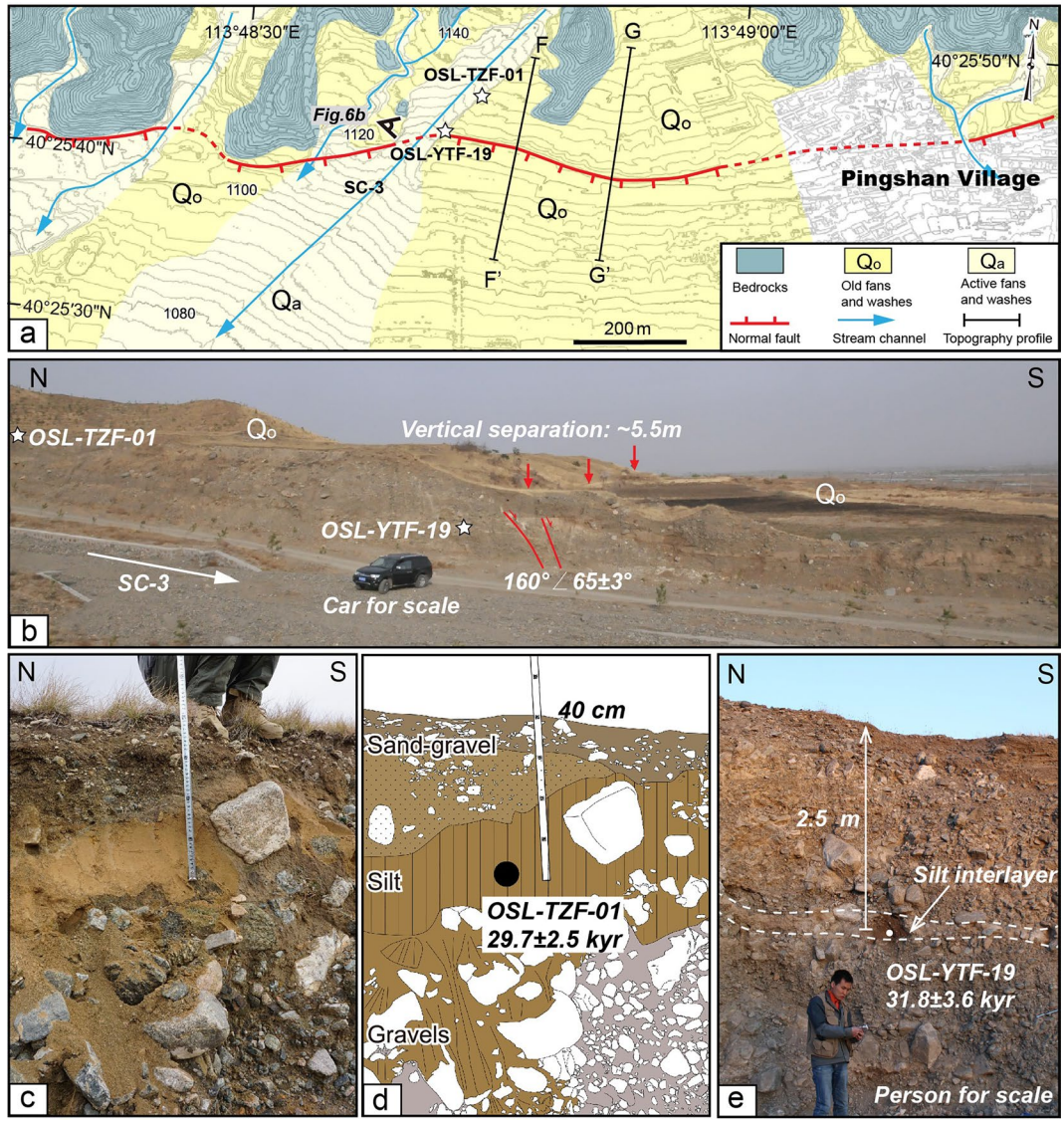

Figure 6. Displaced geomorphic features along the fault trace at Site 3. (a) Contour map showing the Quaternary geomorphic surfaces, fault traces, the location of topographic profiles, and samples (white stars). The topographic contour interval is 2 m. (b) Field photo showing the displaced geomorphic features and the location of samples. Red arrows indicate the fault location. (c), (d), and (e) Field photos and corresponding interpretations showing deposition characteristics and optically stimulated luminescence (OSL) ages of the collected sample.

was distinctly displaced by a south-facing fault (dipping at 70 ± 3°) with a thin loess layer deposited on the hanging wall (Figure 9c). UAV survey data yielded vertical separations of 3.9 ± 0.3, 3.2 + 0.3/−0.4, and 3.8 + 0.3/−0.2 m and cumulative dip-slip magnitudes of 4.0 + 0.4/−0.3, 3.3 + 0.4/−0.5, and 4.0 ± 0.3 m, respectively (Figure S7 in Data Set S1).

4.1.7. Site 7: Q_o

Site seven is near Xuesandun village (Figure 2b) and had fault scarps with distinct linear features on the Q_o alluvial fan in the piedmont. The fault scarp strikes NNE and is expressed as a ~50 m long topographic step between SC-6 and the quarry in the north (Figure 10a). At the base of the scarp, a fault exposure was found that formed a contact between bedrock and late Pleistocene alluvial sediments, dipping 54 ± 3° to SE (Figures 10d and 10e). Figure 10b shows the topographic features of the study site. A topographic profile across the scarp yielded a vertical separation of 6.3 + 0.4/−0.3 m and a dip-slip offset of 7.0 + 0.6/−0.5 m (Figures 10a, 10h). To constrain the abandonment age of the Q_o fan, we collected an OSL sample (OSL-YTF-23)

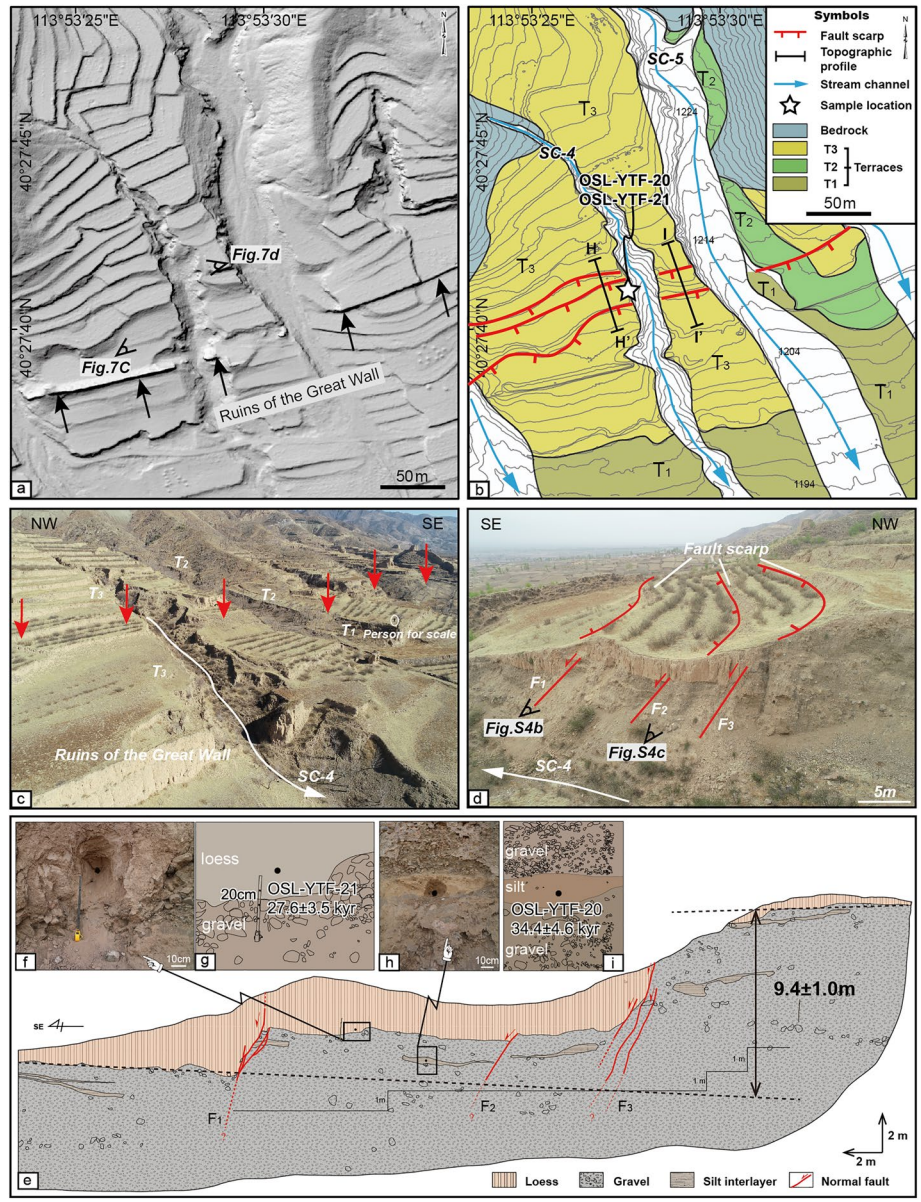

Figure 7. Displaced geomorphic features along the fault trace at Site 4. (a) Hillshade map and (b) Topographic contour map with a contour interval of 2 m, showing the Quaternary geomorphic surfaces, fault traces, the location of topographic profiles. The Black arrows represent the ruins of the Great Wall. (c) and (d) Photos taken by UAVs showing the displaced geomorphic features and fault profiles on the west wall of SC-4. Red arrows indicate the location of the YTF. The loess–gravel contact has been displaced vertically by a group of faults with similar geometry (F_1–F_3). (e) Sketch of the fault zone on the west wall of SC-4 based on the high-resolution orthophoto mosaics image derived by SfM. The original image is shown in Figure S4a in Data Set S1. The black dashed lines are the piercing lines used to measure the vertical displacement. (f), (g), (h), and (i) Field photos and corresponding illustrations showing the location of OSL samples.

from an alluvial silt-sand layer approximately 1.4 m below the fan tread. It yielded an age of 26.3 ± 2.6 kyr (Figures 10f and 10g).

4.2. Ages of Geomorphic Surface

Climate-driven geomorphic surfaces represent ideal strain markers to record the kinematics of active deformation, because of their lateral continuity and the potential to date their formation (Rood et al., 2011). In

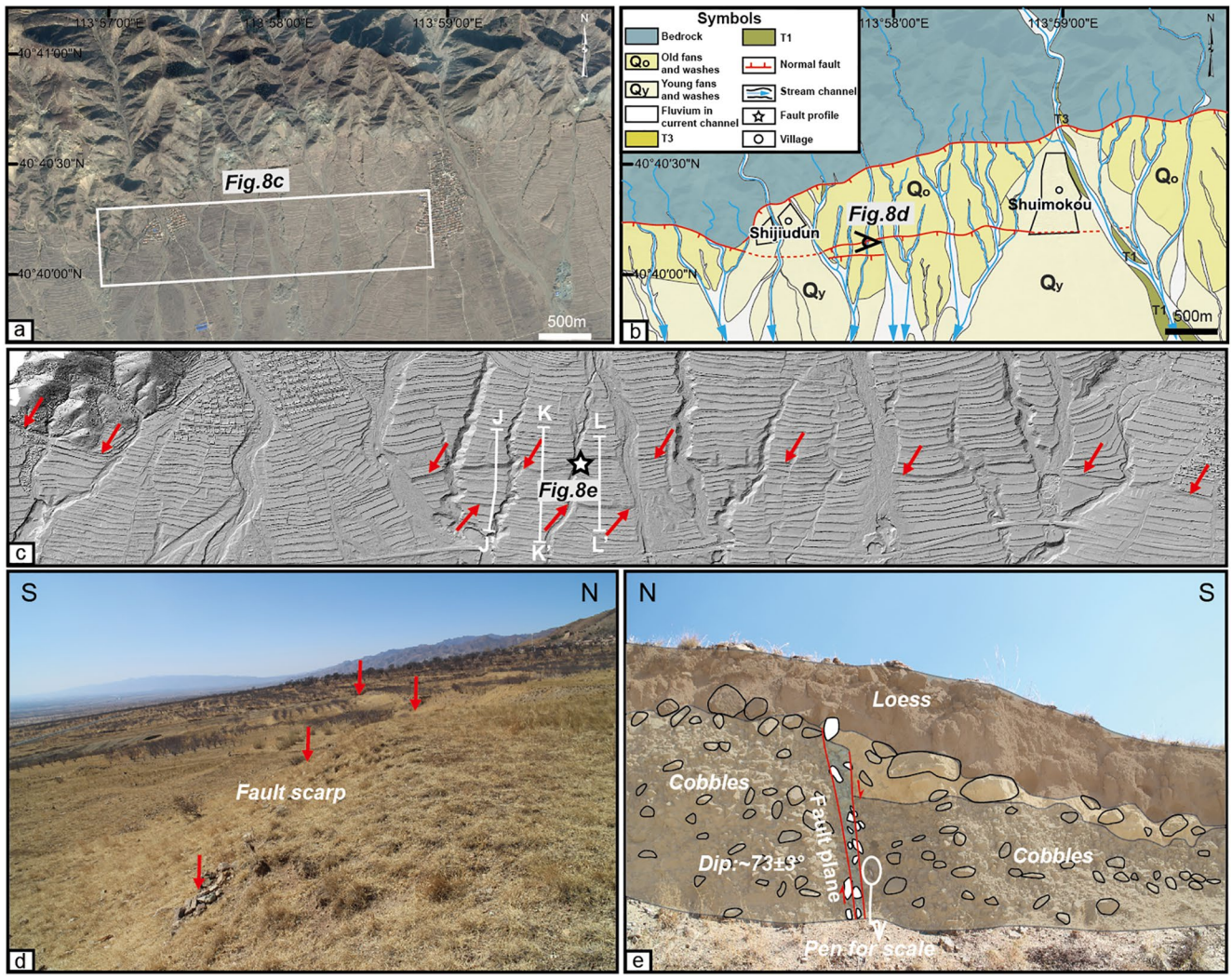

Figure 8. Displaced geomorphic features along the fault trace at Site 5. (a) Google Earth image shows the linear fault trace and the fault scarps on the alluvial fan surface (Q_o) between Shijiudun and Shuimokou villages. The white rectangular box shows the location of panel (c). (b) The Quaternary map showing fault traces and offset alluvial fans. (c) Hillshade map showing fault scarps and locations of topographic profiles. Red arrows indicate the fault location. (d) Field photo showing fault scarps on the alluvial fans. Red arrows indicate the fault location. The perspective of the photo is shown in panel (b). (e) Field photo of fault outcrop. Note that the cobbles are aligned along the fault plane. The perspective of the photo is shown in panel (c).

this study, we found that the T_3 terrace at Site 4 had a sedimentary structure similar to the Q_o alluvial fans at Sites 5 and 6. Moreover, our OSL dating results showed that the age of the T_3 terrace was also similar to that of the Q_o alluvial fans (e.g., Sites 3 and 4). This suggests that the T_3 terraces are contemporaneous with the Q_o alluvial fans. In addition to our five OSL samples, we also reviewed published geochronological studies in the northern SG to strengthen our dating results and attempt to establish a chronological framework for the T_3 terraces and their contemporaneous alluvial fans. Xu et al. (1996) proposed that the formation of multi-stage alluvial fans and terraces in the northern SG was primarily the result of changes of late Quaternary paleoclimate conditions. The stages and structures of the geomorphic surfaces developed in the YTB are comparable to those developed in other basins in the northern SG. Quaternary geochronological work concerning these geomorphic surfaces has been carried out in recent decades (Wang, 2012; Xu et al., 1996, 2011; Zhao, 2013). We compiled the available OSL and ^{14}C ages data in Table S3 in Data Set S1. Although these alluvial fans and fluvial terraces where the samples were collected have been named by different researchers in different ways, they share a similar sedimentary structure that is delineated by underlying alluvium with a loess cover (Figure S8 in Data Set S1). These samples, either taken from the top of the alluvium or the base of the loess layer, yielded ages ranging from 26.7 ± 2.2 kyr to 34.8 ± 2.9 kyr

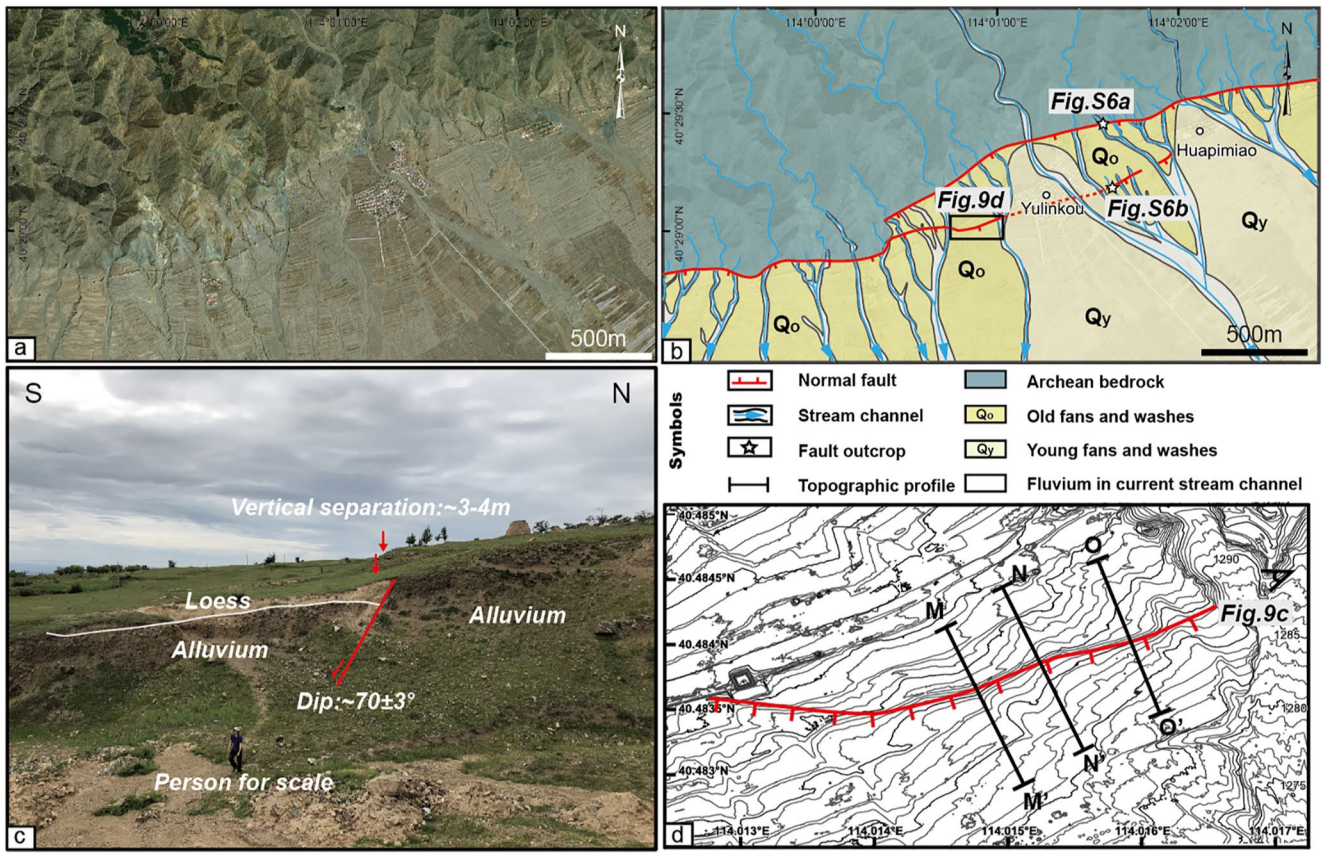

Figure 9. Displaced geomorphic features along the fault trace at Site 6. (a) ArcGIS image showing the geomorphic features around Yulinkou village. (b) Illustration showing the division of alluvial fans, and fault traces. The black rectangular box shows the location of panel (d). (c) Field photo showing the depositing structure of the deformed alluvial fan. Red arrows indicate the location of fault scarps. (d) Topographic contour map with a contour interval of 1 m, showing the linear fault trace and locations of topographic profiles.

(Figure 11). Due to poor bleaching caused by the short duration of flash flood flows, we acknowledge that using the SMAR protocol may overestimate some of the ages in this study (Kunz et al., 2014; Medialdea et al., 2011; Thompson et al., 2018). However, within uncertainty, OSL ages using the SMAR protocol were similar to OSL ages using the SAR protocol and the ^{14}C age. Together, these ages define a best-estimate age of 31.7 ± 1.4 kyr (95% confidence) (Figure 11). Therefore, this stage of alluvial fan and fluvial terrace in the northern SG most likely formed at the end of the relatively warm and wet interglacial stage of the last glacial period (MIS 3: 57–29 kyr; Lisiecki & Raymo, 2005). The overlying loess layer accumulated in the subsequent cold and dry Last Glacial Maximum (MIS 2). This best-estimate age was used in our slip-rate calculation.

4.3. Surface Fault Slip Rate

We selected sites with larger scarps to avoid uncertainties related to the seismic cycle because larger scarps likely experienced multiple major earthquakes (Styron, 2019). At sites with multiple topographic profiles on the same geomorphic surface, we selected the one with the larger offset to calculate slip rates as erosion will reduce the height of the fault scarp. For example, we used the results of topographic profile D–D' on terrace T_3 as the fault displacement at Site 1. The vertical separation and dip-slip offset were divided by the best-estimate age (31.7 ± 1.4 kyr), to derive a surface vertical slip rate and a dip-slip rate. The vertical slip and dip-slip rates of all the sites can be found in Table 2 and Figure S9 in Data Set S1. Notably, both the vertical slip and the dip-slip rates along the fault trace at Sites 5 and 6 should be higher than our estimates because only the fault scarps on one branch of the fault zone were measured (Figures 8 and 9b).

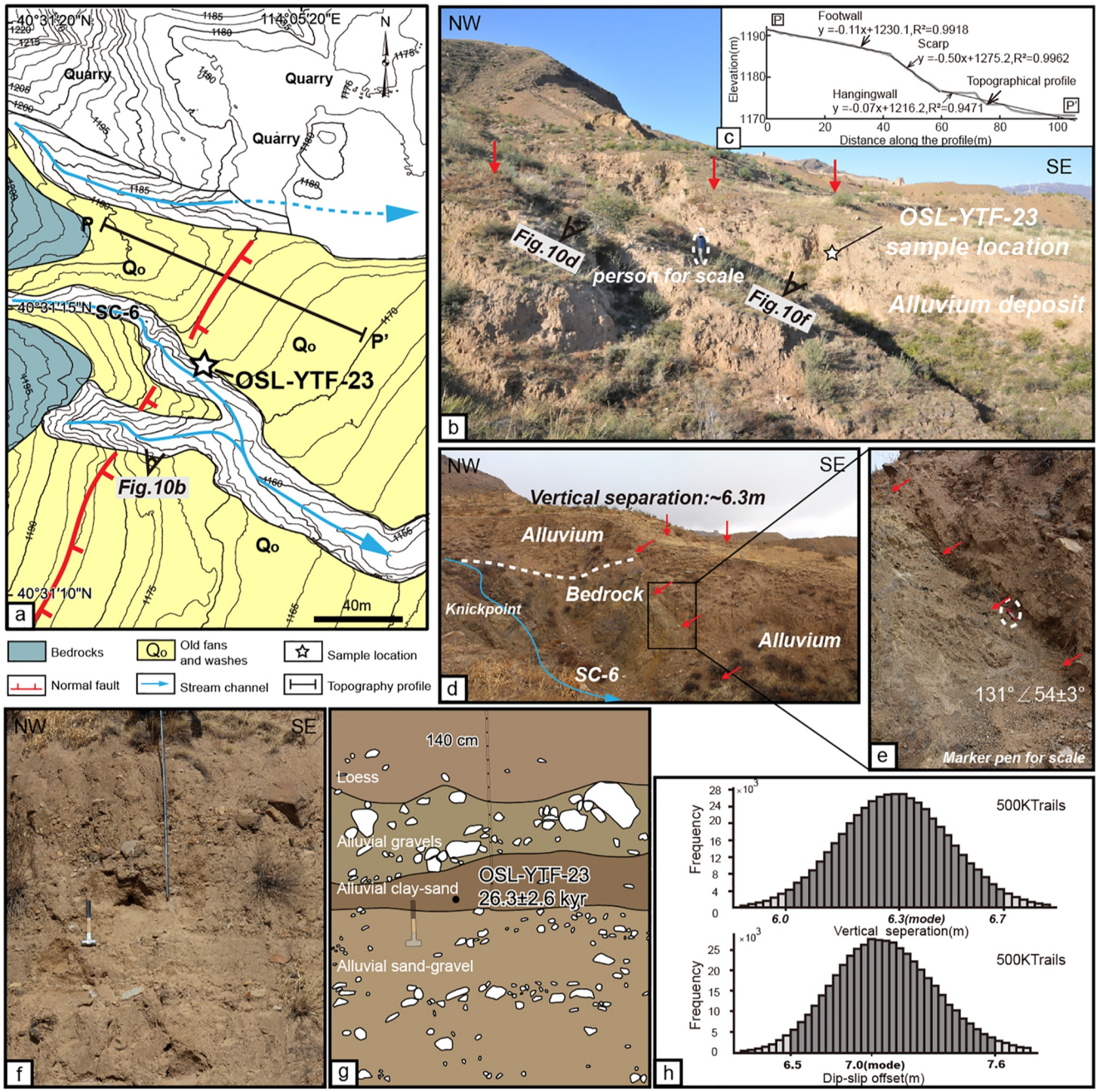

Figure 10. Displaced geomorphic features along the fault trace at Site 7. (a) Illustration of geomorphic units. The topographic contour interval is 2.5 m. (b) Field photo showing the deformed alluvial fan. Red arrows indicate the fault location. (c) The topographic profile used to calculate fault scarp height and displacement. (d) and (e) Field photos showing the fault scarp, knickpoint, and fault outcrop. Red arrows indicate the fault location and fault plane. (f) and (g) Field photos and corresponding illustrations showing the location of OSL samples. (h) Frequency histograms of vertical separation and dip-slip offset from Monte Carlo simulations.

4.4. Morphometric Analysis

The extracted footwall catchments that drain across the YTF are shown in the plan-view map in Figure 2a. Overall, the basins show a symmetrical map-view catchment pattern with larger basins occurring near the fault strike center and smaller basins occurring toward the fault tips (Figure 12a). A positive correlation was also observed between the length of the main stream and the area of the drainage basin (Figure 12b). With the exception of stream No. 4, all of the streams close to the fault strike center (No. 7–9) were long

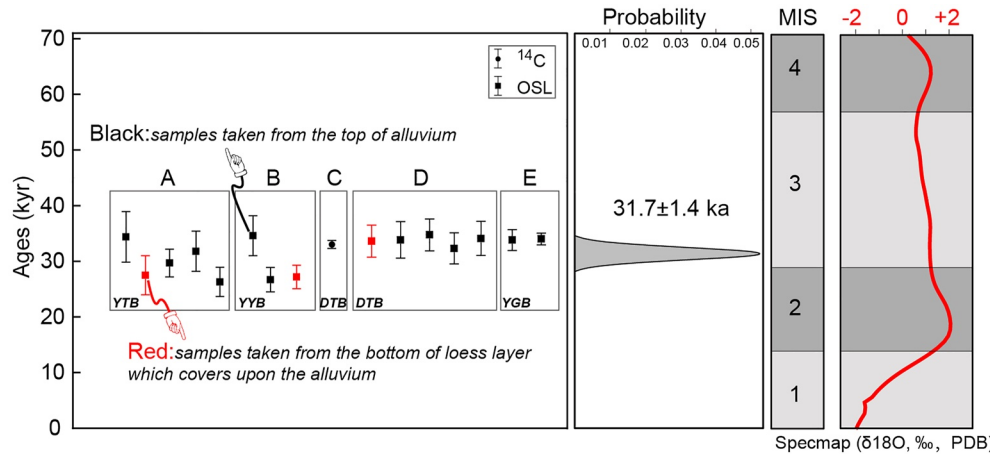

Figure 11. Quaternary dating results of the studied geomorphic marker. Left: Ages of samples in this study and published literature; A–this study, B–Sun, 2018, C–Xu et al., 2011; D–Zhao, 2013; E—Wang, 2012. Middle: the best-fit age given by Monte Carlo simulation assuming all ages obey a Gaussian distribution. Right: SPECMAP marine isotope stages (Lisiecki & Raymo, 2005).

(Figure 12b). We also calculated the relief (maximum elevation minus the minimum elevation) of each drainage basin (Figure 12c) and found that relief peaked near the fault strike center and decreased monotonically toward both ends of the fault.

To reveal the potential along-strike variations in the analyzed indices, we plotted them against the distance from the western fault tip (Figure 13). Notably, the A_f index measures the absolute value of A_f-50 (i.e., $|A_f\text{-}50|$); a detailed explanation is given in Text S2 in Data Set S1. The determined $|A_f\text{-}50|$s were between 0.24 and 21.06 (basin No. 13 and 3, respectively). For comparison, we grouped the basins into three classes: Class 1 ($|A_f\text{-}50| \geq 15$; strongly tilted), Class 2 ($7 \leq |A_f\text{-}50| < 15$; moderately tilted), and Class 3 ($|A_f\text{-}50| < 7$; relatively

Table 2
Topographic Survey Results and Slip Rates

Study Site	Fault dip (°)	Distance along the fault (km)	Topographic profile	Vertical separation (m)	Dip-slip offset (m)	Surface vertical slip rate (mm/yr)	Surface dip-slip rate (mm/yr)	Extension rate at seismogenic depths (mm/yr)
Site 1	50 ± 3	20	A-A′(T_4)	11.1 + 0.7/-1.0				
			B-B′(T_2)	2.5 ± 0.3				
			C-C′(T_3)	2.4 + 0.5/-0.3	2.8 + 0.5/-0.6			
			D-D′(T_3)	3.1 ± 0.2	3.6 + 0.4/-0.3	0.10 ± 0.01	0.11 + 0.02/-0.01	0.17 + 0.05/-0.06
Site 2	68 ± 3	24	E-E′(Q_o)	6.5 + 0.6/-0.3	6.8 + 0.7/-0.5	0.21 ± 0.02	0.22 ± 0.03	0.32 + 0.09/-0.11
Site 3	65 ± 3	29	F-F′(Q_o)	5.4 + 0.2/-0.1	5.7 + 0.4/-0.2			
		29.2	G-G′(Q_o)	5.5 + 0.5/-0.4	5.8 + 0.6/-0.4	0.18 + 0.01/-0.02	0.18 + 0.02/-0.01	0.27 + 0.03/-0.02
Site 4	54 ± 3	36.5	H-H′(T_3)	8.2 + 0.6/-0.4	9.9 + 0.9/-0.7			
		36.6	I-I′(T_3)	9.8 + 0.4/-0.3	11.8 + 0.8/-0.7	0.31 ± 0.01	0.37 + 0.03/-0.02	0.55 + 0.04/-0.03
Site 5	73 ± 3	42	J-J′(Q_o)	7.2 + 1.0/-1.1	7.4 + 1.0/-1.2	>0.23 ± 0.04	>0.23 ± 0.04	>0.34 + 0.06/-0.05
		42.2	K-K′(Q_o)	4.4 + 0.6/-0.8	4.4 ± 0.7			
		42.3	L-L′(Q_o)	4.4 ± 1.2	4.4 + 1.3/-1.2			
Site 6	70 ± 3	47	M-M′(Q_o)	3.9 ± 0.3	4.0 + 0.4/-0.3	>0.12 + 0.02/-0.01	>0.13 + 0.01/-0.02	>0.19 + 0.05/-0.07
		47.2	N-N′(Q_o)	3.2 + 0.3/-0.4	3.3 + 0.4/-0.5			
		47.3	O-O′(Q_o)	3.8 + 0.3/-0.2	4.0 ± 0.3			
Site 7	54 ± 3	58	P-P′(Q_o)	6.3 + 0.4/-0.3	7.0 + 0.6/-0.5	0.24 ± 0.03	0.26 + 0.05/-0.02	0.40 + 0.11/-0.14

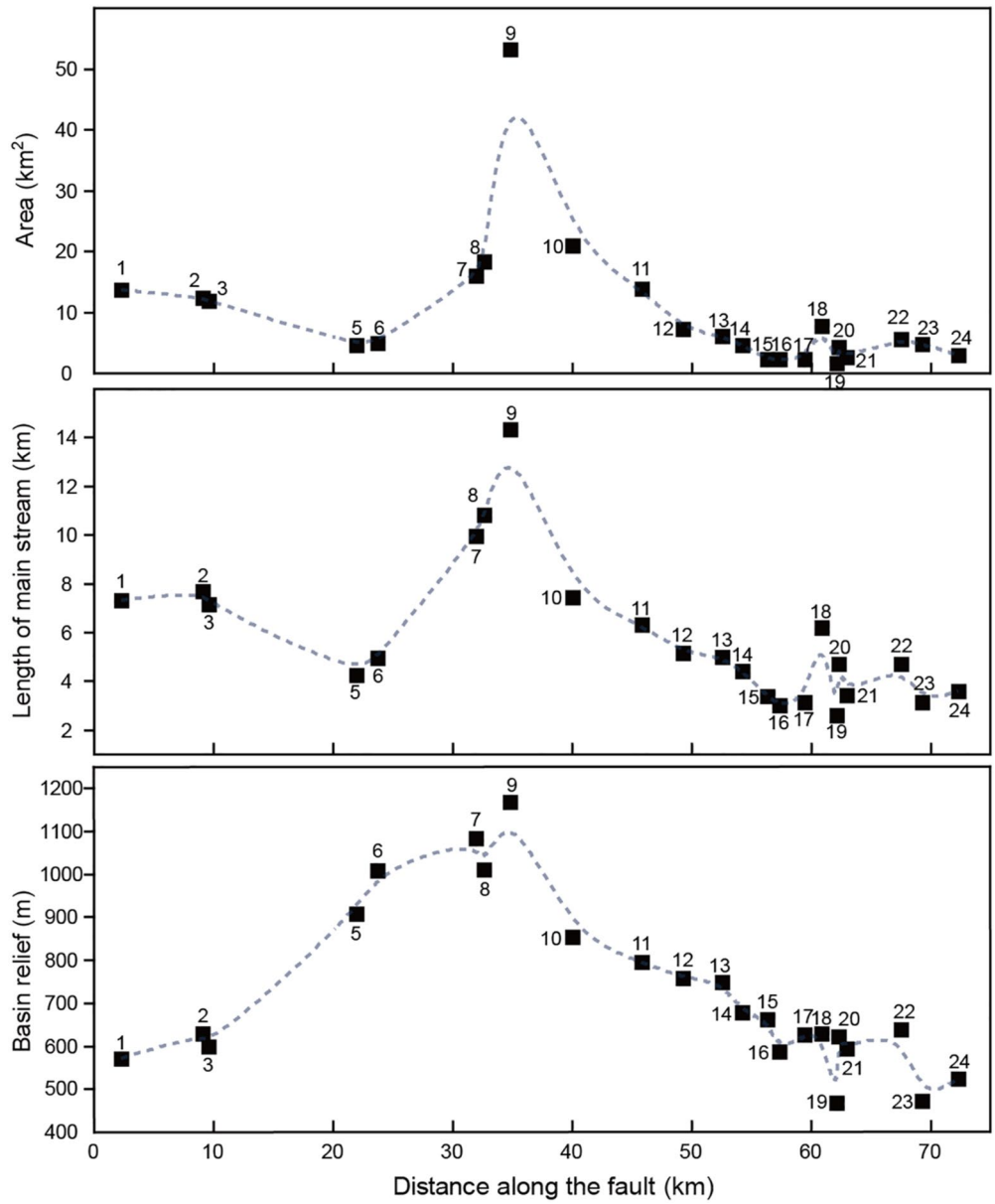

Figure 12. Footwall morphometric parameters; basin area, relief, and length of the main stream of each basin. Data from Table S6 in Data Set S1.

weakly tilted). The obtained HI values varied from 0.30 to 0.57 and were divided into three classes according to the criteria for the classification of HI in terms of reflecting tectonic activity proposed by Hamdouni et al. (2008): Class 1 (HI > 0.5; high tectonic activity), Class 2 (0.4 ≤ HI ≤ 0.5; moderate tectonic activity), and Class 3 (HI < 0.4; relatively weak tectonic activity). Basins No. 1 and 24 were located at the tips of the fault and had values of HI < 0.4, so were defined as Class 3 basins. However, all of the other basins belonged to Class 1 and 2, and had very similar HI values. The V_f values ranged from 0.13 to 1.77 and were divided into three classes: Class 1 (V_f < 0.5; high tectonic slip-rate), Class 2 (0.5 ≤ V_f < 1.0; moderate tectonic slip-rate), and Class 3 (V_f ≥ 1.0; relatively low tectonic slip-rate). It is worth noting that basins with high V_f values were distributed in the fault tips (basin No. 1, 23, and 24) and segmentation boundaries (basin No.14), while basins with low V_f values were distributed at the center of each fault segment. The R_e values were 0.497–0.838 and were grouped into three classes according to Rimando and Schoenbohm (2020): Class 1 (R_e < 0.6; high tectonic activity), Class 2 (0.6 ≤ R_e ≤ 0.8; moderate tectonic activity), and Class 3 (R_e > 0.8; low tectonic activity).

10.1029/2020TC006593

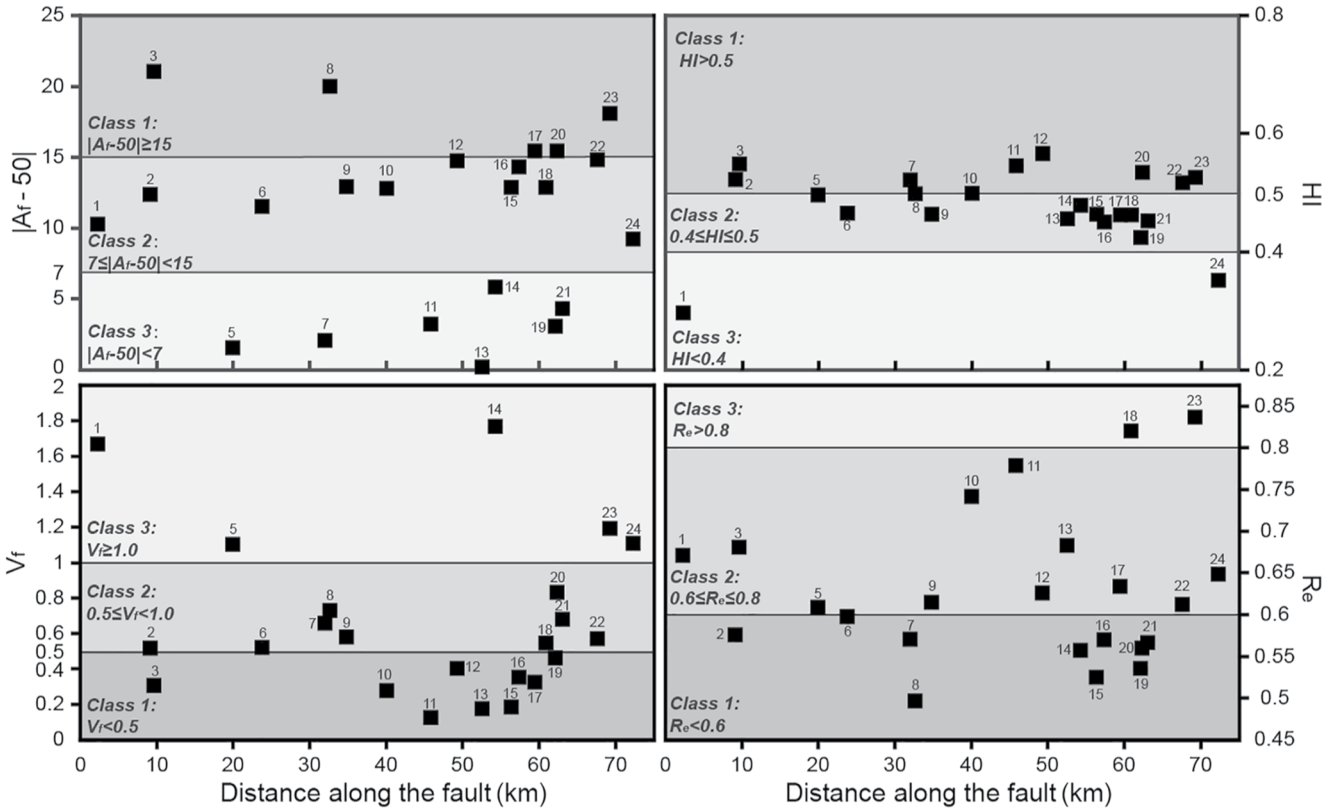

Figure 13. Values and classifications of measured geomorphic indices. Class 1—high tectonic activity; Class 2—moderate tectonic activity; Class 3—low tectonic activity. Data from Table S6 in Data Set S1.

The heart-shaped basins No. 18 and 23 had high R_e values. The S_{mf} index was determined in six different segments along the fault (Figure S10 in Data Set S1) and the observed values were between 1.04 and 1.17 (Table S5 in Data Set S1). According to Hamdouni et al. (2008), all segments belonged to Class 1 ($S_{mf} < 1.1$; high tectonic activity) or Class 2 ($1.1 \le S_{mf} \le 1.5$; moderate tectonic activity), and no segment belonged to Class 3 ($S_{mf} > 1.5$; relatively low tectonic activity). Segments 3 and 4 had lower S_{mf} values than the other segments. The values of Iat for the 23 drainage basins in the study area were summarized in Figure 14 (see Figure 2 for basin locations). Basins with high values of Iat mainly primarily occurred in the fault tips and fault segment boundaries, while basins with a low value of Iat occurred in the center of the whole fault trace and each fault segment.

5. Discussion

5.1. Extension Rates and Implications for Regional Deformation

Normal faulting is always associated with horizontal extension (Jackson, 1987), and estimation of the horizontal extension rate is crucial for understanding the manner of crustal stretching (Zuo et al., 2021). At the near-surface, dip-slip rates can be converted to horizontal extension rates by simple trigonometry; $u_h = u_{dip} \cos \delta$, where u_h is surface extension rate, u_{dip} is the near-surface dip-slip rate, and δ is the near-surface fault dip. However, notably, the coseismic or cumulative slip measured at the ground surface is only a fraction of the actual slip generated by large earthquakes ($M \ge 5.5$) at depth (Manighetti et al., 2007). In addition, many moderate and small earthquakes ($M < 5.5$) related to tectonic extension do not rupture the earth surface. Thus, there are differences between the near-surface dip-slip and the actual net dip-slip at seismogenic depths (6–15 km; Jackson, 1987). The average dip-slip offset generated by large and moderate earthquakes is approximately 1.6 times greater than the average surface-measured fault displacement, while small earthquakes without extensional deformation at the ground surface induce nearly 1/3 of the

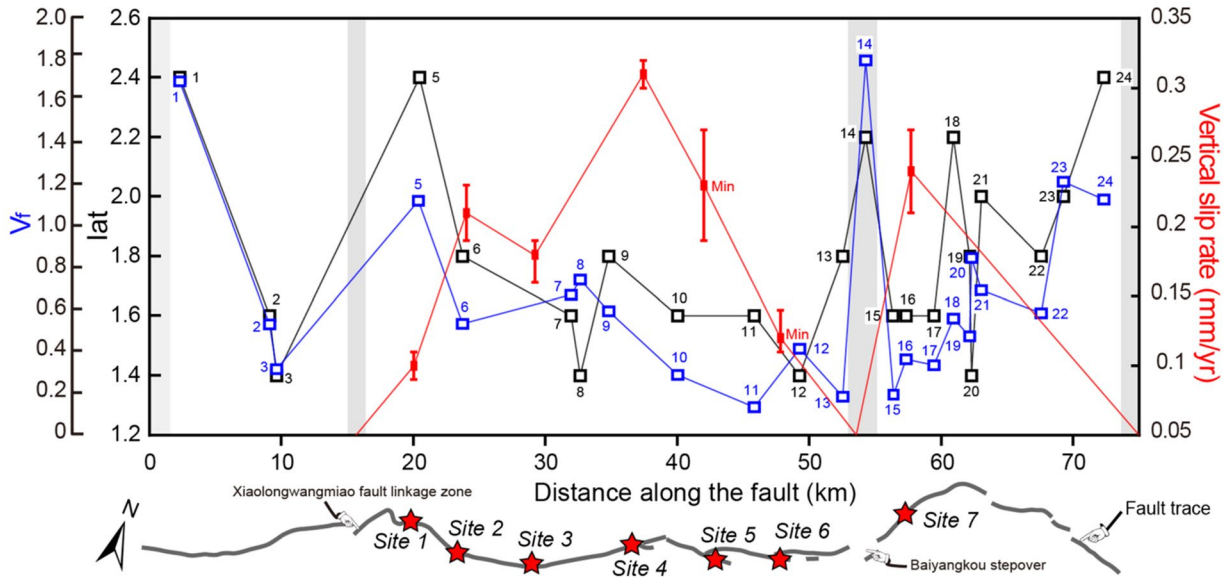

Figure 14. The distribution pattern of the values of Iat (black squares), V_f (blue squares), and the vertical slip rates (red dots with error bars). The regions shaded in gray are fault tip and fault linkage zones. The red stars are study sites in this work. Data refer to Table 2 and Table S6 in Data Set S1.

near-surface dip-slip (Wells & Coppersmith, 1994; Villamor & Berryman, 2001; Zuo et al., 2021). When summing these two parts, we obtained the net fault dip-slip values at seismogenic depths.

To acquire the extension rate at seismogenic depths, we estimated the fault dip angle (α_{seis}) at the seismogenic depth. Jackson (1987) and Jackson and White (1989) demonstrated that the overwhelming majority of worldwide large normal-faulting earthquakes can only occur on normal faults dipping between 30 and 60°. We observed exposed fault planes at more than 30 localities along the fault trace and found that the majority of dips were between 40 and 70° (Figure S11; Table S1 in Data Set S1). Seismological observations suggest that fault planes can flatten with increasing depth and even become approximately planar at mid-crustal depths (Jackson, 1987). The magnetotelluric model proposed by Zhang et al. (2016) also suggests that the YTF tends to flatten at a depth of 10–15 km (Figure S12 in Data Set S1). Thus, we used a fault dip angle of 40 ± 10° in the extension rate calculation at seismogenic depths. As shown in Table 2 and Figure S9 in Data Set S1, the derived extension rates of Sites 1 to 7 at seismogenic depths were 0.17 + 0.05/−0.06, 0.32 + 0.09/−0.11, 0.27 + 0.03/−0.02, 0.55 + 0.04/−0.03, >0.34 + 0.06/−0.05, >0.19 + 0.05/−0.07, and 0.40 + 0.11/−0.14 mm/yr, respectively (95% confidence interval).

Previous researchers have shown that total extension rates across the northern SG are between 1 and 2 mm/yr (Middleton et al., 2017; Zhao et al., 2017). For example, Middleton et al. (2017) obtained extension rates of 1.1–1.8 mm/yr from the geological method (10^4–10^5 yr time-scale) and a seismic extension rate of ~1.1 mm/yr from Kostrov summations of historical earthquakes (10^2–10^3 yr time-scale). Extension rates of ~1.4 and 1.3–1.7 mm/yr were also determined by Middleton et al. (2017) and Zhao et al. (2017), respectively, using GPS measurement (10 years time-scale). In this study, we estimated a maximum extension rate of 0.55 + 0.04/-0.03 mm/yr in the middle of the YTF. Assuming a uniform distribution PDF between 1 and 2 mm/yr for the total extension rate across the northern SG, the YTF accounts for up to 28%–54% of the total crustal extension of the northern SG (95% confidence). Our data suggest that the YTF is an important structure for accommodating the extension strain in the northern SG. Given the along-strike gradients in extension rates along the fault strike, we believe that different parts of the YTF played different roles in accommodating the extension strain in the northern SG. Based on the minimum extension rate of 0.17 + 0.05/−0.06 mm/yr, we determined that the YTF accounts for at least 10% of the total crustal extension of the northern SG. Previous studies have determined significantly different geological rates for other faults in this region, for example the Liulengshan Fault and the Yuguang Basin Fault (Figure 1b). Therefore, this study only discusses the YTF.

5.2. Implications for the Along-Strike Variations in Fault Activity

Active normal faults have a distinct topographic expression, particularly in terms of their footwall topography (Densmore et al., 2004; Whittaker & Walker, 2015). We found that the footwall block shows a nearly symmetric drainage basin pattern in plan-view when excluding antecedent basin No. 4. Of the basins that developed in response to fault displacement, the largest basins are at the center of the whole fault strike and subsegment, while small basins are found toward the fault tips (Figure 12a). The length of each basin's main stream follows the same relationship, with the length of the stream decreasing from the center of the fault strike out to the fault tips. This is in accordance with the general form of the relationship between stream length and drainage area; $Ls = cA^b$ (Hack, 1957; Hovius, 1996), where Ls is the stream length, A is the drainage area, and b and c are constants for a given set of drainage basins (Figure 12b). Similarly, basin relief also peaks at the fault center and decreases toward the ends of the fault (Figure 12c). It is likely that basin relief is jointly influenced by antecedent pre-faulting topography and later tectonic uplift. Previous studies have established an empirical scaling relationship between fault length and accumulative displacement; $d = \gamma l$, where d is the fault displacement, l is the fault length, and γ varies from 0.001 to 0.1 (Dawers et al., 1993; Cowie & Roberts, 2001; Kim & Sanderson, 2005). For example, for active normal faults in the northeastern Basin and Range Province, $\gamma = 0.033$ (Densmore et al., 2004). Adopt a ratio of $d/l = 0.033$, the fault displacement generated by the ~75 km long YTF is approximately 2.5 km, which is larger than the sum of the maximum footwall relief (~1.2 km) and basin thickness (0.5 km) (Zheng et al., 2000). Thus, we believe that the along-strike variations in basin relief reflect the differential uplift of the bedrock along the fault. The distribution of the basin area appears to mimic the widely held belief that large basins occur near the strike center of the fault, which has a larger fault displacement (Densmore et al., 2004). Together, the distribution pattern of the area and relief of the drainage basin implies that the most prominent fault activity center is likely located at the middle of the fault (approximately between outlets of basins No. 7–10) (Figure 2a) and the level of fault activity decreases toward the fault tips.

Figure 14 shows a plot of the vertical slip rate, Iat, and V_f values versus the distance along fault strike. As mentioned above, the slip rates of the fault segments at Sites 5 and 6 may be greater than our estimations, therefore they are labeled as minimum rates in the figure. In addition, the value of slip rate at the fault boundaries was set to 0, indicating no vertical displacement at those localities. As shown in Figure 14, the overall trend of Iat and V_f was relatively consistent, despite the differences in some drainage basins (e.g., basins No. 7–9, 12, 21). Both Iat and V_f were lower at the center of each fault subsegment and higher at the tips of the fault, indicating that the level of fault activity was higher at the fault center and decreased toward the fault boundaries. In addition, the lowest value of V_f appeared near the center of the entire fault (basin No. 11). The Iat index was not as evident as V_f because there were two minima in the middle of the fault (basins No. 8 and 12). Together with the drainage basin pattern (Figure 12), we propose that the long-standing fault activity center is located near the middle of the fault and the level of fault activity decreases toward the fault tips. As confirmed by our scattered geological data, the vertical slip rates in the central portion (e.g., Site 4) are also much higher than those on the two flanks. This pattern resembles the idealized long-term deformation pattern of an individual fault zone; that is, cumulative displacement is generally highest at the center of a fault and decreases toward the fault tips (Kim & Sanderson, 2005). In addition, we note that our measured Iat and V_f values overall show a negative correlation with the vertical slip rate, which conforms to the inversely proportional relationship between Iat and V_f, and the slip rate illustrated in Section 3.4 (Figure 14). This indicates that the analysis of geomorphic indices can be an effective tool for assessing the relative tectonic activity along an active fault. The inconsistencies in the values of Iat and V_f are likely due to the scarcity of geological slip rates, and the errors in the measurement of geomorphic parameters.

Our estimations of slip rate and measurements of geomorphic indices jointly indicate that the level of fault activity is highly heterogeneous and fluctuates along the fault strike (Figure 14). This can be attributed to fault segmentation and linkage, the dip of fault planes, and fault kinematics. The along-strike gradients in the fault activity of the YTF correlated well with its fault geometric barriers; for example, the Baiyangkou stepover and the Xiaolongmwangmiao fault linkage zone (Figure 14). This indicates that the YTF may have evolved from isolated fault segments through fault growth and linkage. Differences in the fault dip may lead to spatial variations in the fault displacements. Horizontal extension by normal faulting typically results in arrays of fault-bounded blocks that rotate about the horizontal axes as their bounding faults

slip (Jackson & Mckenzie, 1983; Leeder & Jackson, 1993; Proffett, 1977). This has long been recognized in extensional tectonic regimes both in coseismic surface deformation (e.g., Perouse et al., 2018) and field outcrop-scale observations (Rao et al., 2019). As evidenced by numerical modeling (Buck, 1988), normal faults are typically characterized by the sequential development of fault blocks (Jackson, 1987). This means that some faults are progressively rotated to lower dips and may eventually become locked, forming a new generation of steeper-dipping faults. Evidently, fault segment with the highest fault activity, indicated by the values of Iat and V_f, was between basins No. 11 and 12. This is not fully consistent with the drainage basin pattern and the determined fault slip rate which indicated that the highest fault activity was between the outlets of basins No. 7–10. Field observations revealed steeper dipping fault planes in the basin than at the range front (e.g., Sites 5 and 6; Figure S6 in Data Set S1) which may have caused the aforementioned inconsistency. However, overall, there were no substantial differences in fault dips along the fault, based on our field observations (Figure S11 in Data Set S1). Therefore, fault activity is only affected locally by fault dips, and it is not generally significant. For a strike-slip fault, a change in fault geometry may give rise to a vertical component on the fault, causing compression in the restraining bend and extension in the releasing bend. Evidence (e.g., fault plane striations and deflected stream channels across the fault) has shown that the ENE-trending South Xionger Shan Fault and the Huaian Basin Fault may have a sinistral movement (Figure 1b; Duan, 1994; Zhou et al., 2016). Luo et al. (2020) also suggested left-lateral strike-slipping on the WNW-trending segment (Wayaokou to Yiqingpo). If the entire YTF has a left-lateral strike-slip component, then the NWW-trending segment (from Xiaolongwangmiao to Yanjiabu) and NE-trending segment (from Xuesandun to Wayaokou) would constitute a restraining bend and releasing bend, respectively (Figure 2a). This is possible because the YTF is located in the transition zone of the SG and ZBFZ, whereas the latter is dominated by left-laterally strike-slip movement (Xu et al., 1998; Zhang et al., 2018). Additional studies are required to address this key question.

5.3. Implications for Seismic Hazards

The mapped fault traces and determined fault slip rates, as well as previous paleoearthquake studies during the late Quaternary, provide insights into seismic hazards along the YTF. Hence, it was first necessary to estimate the possible range of earthquake magnitude that YTF could generate. As we think that the vertical offset of T_3 terrace at Site 1 may be better represented by the D-D' profile (3.1 ± 0.2 m) than the C-C' topographic profile (2.4 + 0.5/-0.3 m), the minimum offset measured in this study (2.5 ± 0.3 m) was on the fault scarp on the T_2 terrace at Site 1 along the B–B' topographic profile. However, it is necessary to assess whether this minimum offset corresponds to single or multiple earthquake events. The formation age of T_2 has been constrained to be 12.5 ± 1.6 kyr, by an OSL sample collected from the silt interlayer between the T_2 gravels approximately 0.4 m below the T_2 surface (Luo et al., 2020; Figure 4a). Therefore, the 2.5 ± 0.3 m offset of T_2 terrace should have occurred over the last 12.5 ± 1.6 kyr. The excavated trench about 5 km east of this locality revealed that the most recent event occurred about 7.9 ± 0.1 kyr ago (^{14}C dating; Xu et al., 2002). Therefore, the 2.5 ± 0.3 m offset of T_2 was highly likely due to the accumulation of multiple events. Consequently, we cannot use displacement versus earthquake magnitude scaling relationships (Wells & Coppersmith, 1994) to estimate the seismic potential. An alternative method to estimating seismic potential is the relationship between surface rupture length (L) and earthquake magnitude for normal faults; $Mw = 4.86 + 1.32\log10(L)$ (Wells & Coppersmith, 1994). If it is assumed that the entire length of the Holocene active fault segment east of Xiaolongwangmiao village ruptured (~58 km; Figure 2a), then the above relationship would indicate a magnitude of Mw 7.2. Anderson et al. (1996, 2017, 2021) have revealed that knowledge of the long-term fault-slip rate can improve magnitude estimates. Thus, we can also use the magnitude versus slip rate (S) and fault length (L) scaling relationships of Anderson et al. (1996) to estimate magnitude; $Mw = 5.12 + 1.16\log10(L) - 0.20\log10(S)$. Using this regression, the slip rate we measured, and a maximum surface rupture length of 58 km correlated with earthquake magnitude estimates ranging from Mw 7.2 to 7.3. These estimates are consistent with the magnitude of the 1626 Lingqiu earthquake (M 7.0) (Figure 1b) (Shen & Wang, 1994; Xu et al., 2002). Consequently, the YTF poses a considerable seismic hazard to the Yanggao and Tianzhen Counties (population ~600,000), which are located approximately 5 km from the active YTF fault trace.

Previous paleoseismic studies have also revealed that the average recurrence interval of surface-rupturing earthquakes along the YTF is only approximately 1.5–2.5 kyr (Duan, 1994; Xu et al., 2002). However, there

has not been a surface-rupturing event along the fault since approximately 6–8 kyr, which exceeded the expected recurrence interval (Xu et al., 2002). However, other earlier studies also indicated that the YTF may be the causative fault for the 1673 Tianzhen earthquake with an estimated magnitude of M 6.5; however, limited research has been done on this historical earthquake (Gu et al., 1983; Lee et al., 1976; Li et al., 2007; Wan et al., 2006). Hence, a systematic study of paleoseismic history is required to better assess and reduce the earthquake hazards along the YTF.

6. Conclusions

This study used high-resolution morphotectonic mapping and OSL dating of displaced T_3 terraces and their contemporaneous alluvial fans along the YTF to determine surface vertical slip rates of ~0.10–0.31 mm/yr, dip-slip rates of ~0.11–0.37 mm/yr using field-measured fault dips, and extension rates of ~0.17–0.55 mm/yr assuming a fault dip of 40 ± 10° at seismogenic depths. These estimated extension rates imply that at least 10% and up to 28%–54% of the total extension of the northern SG is inhomogeneously partitioned by different parts of the YTF. Combined with a geomorphic analysis of the footwall topography, we evaluated the spatial pattern of fault activity. Our estimated slip rates and the measured geomorphic indices indicate that the long-standing fault activity center is located at the center of the fault, with the level of fault activity decreasing toward the fault tips. Fault activity is highly heterogeneous and fluctuates along the fault strike, which may be attributed to either fault segmentation and linkage or possible left-lateral movement of the fault. To better understand the active deformation in the northern SG and assess seismic hazards along the YTF, additional research is required to address the fault kinematics and paleoseismic history of the fault.

Data Availability Statement

The DEM data used in the geomorphic analysis were obtained from the 30 m-resolution Advanced Spaceborne Thermal Emission and Reflection Radiometer (ASTER) GDEM (V2), which can be downloaded from the website https://earthexplorer.usgs.gov/. Supplementary text, figures, and tables are provided in Data Set S1. The data availability of this study complies with the FAIR Data standards. All data of OSL dating results, UAV-derived digital elevation models, topographical profiles, and field-measured fault dips related to this study were archived in 4TU. Research Data at https://doi.org/10.4121/13153871 (Luo, 2020).

Acknowledgments
This study was jointly financed by the National Key Research and Development Program of China (2017YFC1500101), the Second Tibetan Plateau Scientific Expedition and Research Program (2019QZKK0901), and the National Natural Science Foundation of China (42002233). The authors thank Dr. Huili Yang and Dr. Junxiang Zhao for their support during the OSL measurements. The authors are grateful to Dr. Jianguo Xiong for his suggestions on our earlier manuscript. The authors also thank Dr. Jiahong Luo for his help in GMT plotting, Dr. Ian Pierce for his help in language polishing, Dr. Zifa Ma for his help in fieldwork, and Dr. Qingri Liu for guidance in Monte Carlo simulations. Lastly, we thank the editors Dr. Taylor Schildgen and Dr. Jessica Thompson Jobe, and Dr. Jeremy Rimando, and other anonymous reviewers for their helpful comments on our manuscript.

References

Anderson, J. G., Biasi, G. P., Angster, S., & Wesnousky, S. G. (2021). Improved scaling relationships for seismic moment and average slip of strike-slip earthquakes incorporating fault-slip rate, fault width, and stress drop. *Bulletin of the Seismological Society of America*, *111*, 2379–2392. https://doi.org/10.1785/0120210113

Anderson, J. G., Biasi, G. P., & Wesnousky, S. G. (2017). Fault-scaling relationships depend on the average fault-slip rate. *Bulletin of the Seismological Society of America*, *107*(6), 2561–2577. https://doi.org/10.1785/0120160361

Anderson, J. G., Wesnousky, S. G., & Stirling. (1996). Earthquake size as a function of fault slip rate. *Bulletin of the Seismological Society of America*, *86*(3), 683–690. https://doi.org/10.1785/bssa08601bs100

Angster, S., Wesnousky, S., Huang, W. L., Kent, G., Nakata, T., & Goto, H. (2016). Application of UAV photography to refining the slip rate on the Pyramid Lake fault zone, Nevada. *Bulletin of the Seismological Society of America*, *106*(2), 785–798. https://doi.org/10.1785/0120150144

Bai, M. K., Chevalier, M. L., Pan, J. W., Replumaz, A., Leloup, P. H., Métois, M., & Li, H. (2018). Southeastward increase of the late Quaternary slip-rate of the Xianshuihe fault, eastern Tibet. Geodynamic and seismic hazard implications. *Earth and Planetary Science Letters*, *485*, 19–31. https://doi.org/10.1016/j.epsl.2017.12.045

Bemis, S. P., Micklethwaite, S., Turner, D., James, M. R., Akciz, S., Thiele, S. T., & Bangash, H. A. (2014). Ground-based and UAV-Based photogrammetry: A multi-scale, high-resolution mapping tool for structural geology and paleoseismology. *Journal of Structural Geology*, *69*, 163–178. https://doi.org/10.1016/j.jsg.2014.10.007

Boulton, S. J., & Stokes, M. (2018). Which DEM is best for analyzing fluvial landscape development in mountainous terrains? *Geomorphology*, *310*, 168–187. https://doi.org/10.1016/j.geomorph.2018.03.002

Buck, W. R. (1988). Flexural rotation of normal faults. *Tectonics*, *7*(5), 959–973. https://doi.org/10.1029/tc007i005p00959

Bull, J. M., Barnes, P. M., Lamarche, G., Sanderson, D. J., Cowie, P. A., Taylor, S. K., & Dix, J. K. (2006). High-resolution record of displacement accumulation on an active normal fault: Implications for models of slip accumulation during repeated earthquakes. *Journal of Structural Geology*, *28*, 1146–1166. https://doi.org/10.1016/j.jsg.2006.03.006

Bull, W. B., & McFadden, L. (1977). Tectonic geomorphology North and South of the Garlock fault, California. In D. O. Dohering (Ed.), *Geomorphology in Arid regions* (pp. 115–138): Publication in Geomorphology, State University of New York.

Cheng, Y. L., He, C. Q., Rao, G., Yan, B., Lin, A., Hu, J., et al. (2018). Geomorphological and structural characterization of the southern Weihe Graben, central China: Implications for fault segmentation. *Tectonophysics*, *722*, 11–24. https://doi.org/10.1016/j.tecto.2017.10.024

Cowie, P. A., & Roberts, G. P. (2001). Constraining slip rates and spacings for active normal faults. *Journal of Structural Geology*, *23*(2001), 1901–1915. https://doi.org/10.1016/s0191-8141(01)00036-0

Cowie, P. A., Roberts, G. P., Bull, J. M., & Visini, F. (2012). Relationships between fault geometry, slip rate variability and earthquake recurrence in extensional settings. *Geophysical Journal International*, *189*, 143–160. https://doi.org/10.1111/j.1365-246X.2012.05378.x

Cox, R. T. (1994). Analysis of drainage-basin symmetry as a rapid technique to identify areas of possible Quaternary tilt-block tectonics: An example from the Mississippi Embayment. *The Geological Society of America Bulletin*, *106*, 571–581. https://doi.org/10.1130/0016-7606(1994)106<0571:aodbsa>2.3.co;2

Dawers, N. H., Anders, M. H., & Scholz, C. H. (1993). Growth of normal faults: Displacement-length scaling. *Geology*, *21*, 1107–1110. https://doi.org/10.1130/0091-7613(1993)021<1107:gonfdl>2.3.co;2

Deng, Q. D., Yonekura, N., & Xu, X. W. (1994). Study on the late Quaternary kinematics of the Northern Piedmont Fault of the Liuleng Mountain. *Seismology and Geology*, *16*(4), 339–343.

Densmore, A. L., Dawers, N. H., Gupta, S., Guidon, R., & Golden, T. (2004). Footwall topographic development during continental extension. *Journal of Geophysical Research*, *109*, F03001. https://doi.org/10.1029/2003JF000115

Ding, G. Y., & Lu, Y. C. (1983). Discussion on the basic characteristics of neotectonic deformation in north China block. *North China Earthquake Sciences*, *1*(No.2), 1–9.

Duan, R. T. (1994). *Research on active faults and seismic hazards in Yangyuan Basin and its neighboring area*. Institute of Geology, China Earthquake Administration.

Fang, Z. J., Duan, R. T., Zheng, B. H., & Yang, Z. E. (1994). Research on the activity of the northern margin fault of the Huaian Basin in Hebei Province. *North China Earthquake Sciences*, *12*(4), 25–33.

Friedrich, A. M., Wernicke, B. P., Niemi, N. A., Bennett, R. A., & Davis, J. L. (2003). Comparison of geodetic and geologic data from the Wasatch region, Utah, and implications for the spectral character of Earth deformation at periods of 10 to 10 million years. *Journal of Geophysical Research*, *108*(B4), 2199. https://doi.org/10.1029/2001JB000682

Gu, G. X., Lin, T. H., & Shi, Z. L. (1983). *The Catalogue of Chinese earthquakes (1831 BC-AD 1969)*. Science Publishing House.

Hack, J. T. (1957). *Studies of longitudinal stream profiles in Verginia and Maryland*. US Government Printing Office.

Hamdouni, R. E., Irigaray, C., Fernández, T., Chacón, J., & Keller, E. A. (2008). Assessment of relative active tectonics, southwest border of the Sierra Nevada (southern Spain). *Geomorphology*, *96*(2008), 150–173. https://doi.org/10.1016/j.geomorph.2007.08.004

Hetzel, R., Tao, M. X., Stokes, S., Niedermann, S., Ivy-Ochs, S., Gao, B., et al. (2004). Late Pleistocene//Holocene slip rate of the Zhangye thrust (Qilian Shan, China) and implications for the active growth of the northeastern Tibetan Plateau. *Tectonics*, *23*. https://doi.org/10.1029/2004TC001653

Hovius, N. (1996). Regular spacing of drainage outlets from linear mountain belts. *Basin Research*, *8*, 29–44. https://doi.org/10.1111/j.1365-2117.1996.tb00113.x

Hu, X. F., Cao, X. L., Li, T., Mao, J., Zhang, J., He, X., et al. (2021). Late quaternary fault slip rate within the Qilian Orogen, insight into the deformation kinematics for the NE Tibetan Plateau. *Tectonics*, *40*, e2020TC006586. https://doi.org/10.1029/2020TC006586

Hughes, A., Rood, D. H., Whittaker, A. C., Bell, R. E., Rockwell, T. K., Levy, Y., et al. (2018). Geomorphic evidence for the geometry and slip rate of a young, low-angle thrust fault: Implications for hazard assessment and fault interaction in complex tectonic environments. *Earth and Planetary Science Letters*, *504*, 198–210. https://doi.org/10.1016/j.epsl.2018.10.003

Jackson, J., & McKenzie, D. (1983). The geometrical evolution of normal fault systems. *Journal of Structural Geology*, *5*(5), 471–482. https://doi.org/10.1016/0191-8141(83)90053-6

Jackson, J. A. (1987). Active normal faulting and crustal extension. *Geological Society, London, Special Publications 1987*, *28*, 3–17. https://doi.org/10.1144/GSL.SP.1987.028.01.02

Jackson, J. A., & White, N. J. (1989). Normal faulting in the upper continental crust: Observations from regions of active extension. *Journal of Structural Geology*, *11*(No. 1/2), 15–36. https://doi.org/10.1016/0191-8141(89)90033-3

Johnson, K., Nissen, E., Saripalli, S., Arrowsmith, J. R., McGarey, P., Scharer, K., et al. (2014). Rapid mapping of ultrafine fault zone topography with structure from motion. *Geosphere*, *10*, 969–986. https://doi.org/10.1130/GES01017.1

Kim, Y. S., & Sanderson, D. (2005). The relationship between displacement and length of faults: A review. *Earth-Science Reviews*, *68*, 317–334. https://doi.org/10.1016/j.earscirev.2004.06.003

Kirby, E., & Whipple, K. X. (2012). Expression of active tectonics in erosional landscapes. *Journal of Structural Geology*, *44*, 54–75. https://doi.org/10.1016/j.jsg.2012.07.009

Kunz, A., Pflanz, D., Weniger, T., Urban, B., Krüger, F., & Chen, Y.-G. (2014). Optically stimulated luminescence dating of young fluvial deposits of the middle Elbe river flood plains using different age models. *Geochronometria*, *41*(1), 36–56. https://doi.org/10.2478/s13386-013-0140-7

Lee, W. H. K., Wu, F. T., & Jacobsen, C. (1976). A catalog of historical earthquakes in China compiled from recent Chinese publications. *Bulletin of the Seismological Society of America*, *66*(No.6), 2003–2016. https://doi.org/10.1785/bssa0660062003

Leeder, M. R., & Jackson, J. A. (1993). The interaction between normal faulting and drainage in active extensional basins, with examples from western United States and central Greece. *Basin Research*, *5*, 79–102. https://doi.org/10.1111/j.1365-2117.1993.tb00059.x

Lei, J. H., Li, Y. L., Oskin, M. E., Wang, Y., Xiong, J., Xin, W., et al. (2020). Segmented thrust faulting: Example from the northeastern margin of the Tibetan plateau. *Journal of Geophysical Research: Solid Earth*, *125*, e2019JB018634. https://doi.org/10.1029/2019JB018634

Lei, J. H., Li, Y. L., Ren, Z. K., Xiu, H., Jianguo, X., Fei, L., & Jinrui, L. (2021). Variable thrust rates of the eastern Qilianshan Mountain front, northeastern margin of the Tibet Plateau and its implication to the topography of the Yongchangnan Shan. *Frontiers of Earth Science*, *9*. https://doi.org/10.3389/feart.2021.622568

Li, C. Y., Wang, X. C., He, C. Z., Kong, Z., & Li, X. (2017). *National 1:200 000 digital geological map (open edition) spatial database (V1). Development Research Center of China Geological Survey; China geological survey, 1957*. National Geological Archive of China.

Li, T. M., Shen, Z. K., Xu, J., & Wan, Y. G. (2007). Analysis on the parameters of seismogenic fault of the earthquake more than 6.5 in North China. *Progress in Geophysics*, *22*(No. 1), 95–103.

Li, Y. H., Wang, Q. L., & Cui, D. X. (2013). Research on fault motion and segmentation characteristic of Kouquan Fault in Datong Basin by numerical simulation. *Journal of Geodesy and Geodynamics*, *33*(No.4), 9–12.

Liang, K., Ma, B. Q., Li, D. W., Tian, Q., Sun, C., He, Z., et al. (2019). Quaternary activity of the Zhuozishan West Piedmont Fault provides insight into the structural development of the Wuhai Basin and northwestern Ordos Block, China. *Tectonophysics*, *754*, 56–72. https://doi.org/10.1016/j.tecto.2019.02.004

Lisiecki, L. E., & Raymo, M. E. (2005). A Pliocene-Pleistocene stack of 57 globally distributed benthic $\delta^{18}O$ records. *Paleoceanography*, *20*(PA), 1003. https://doi.org/10.1029/2004PA001071

Lucieer, A., de Jong, S. M., & Turner, D. (2014). Mapping landslide displacements using Structure from Motion (SfM) and image correlation of multi-temporal UAV photography. *Progress in Physical Geography*, *38*(1), 97–116. https://doi.org/10.1177/0309133313515293

Luo, Q. X. (2020). *Associated data underlying the paper: Slip distribution and slip rates of the Yanggao-Tianzhen Fault (northern Shanxi Graben): Insights for regional active deformation*. 4TU.Research Data. https://doi.org/10.4121/13153871.v1
Luo, Q. X., Li, C. Y., Ren, G. X., Li, X., Ma, Z., & Dong, J. (2020). The late Quaternary activity features and slip rate of the Yanggao-Tianzhen Fault. *Seismology and Geology*, *42*(No.2), 399–413. https://doi.org/10.3969/j.issn.0253-4967.2020.02.010
Manighetti, I., Campillo, M., Bouley, S., & Cotton, F. (2007). Earthquake scaling, fault segmentation, and structural maturity. *Earth and Planetary Science Letters*, *253*(3–4), 429–438. https://doi.org/10.1016/j.epsl.2006.11.004
Marliyani, G. I., Arrowsmith, J. R., & Whipple, K. X. (2016). Characterization of slow slip rate faults in humid areas: Cimandiri fault zone, Indonesia. *Journal of Geophysical Research: Earth Surface*, *121*, 2287–2308. https://doi.org/10.1002/2016JF003846
Medialdea, A., Porat, N., & Benito, G. (2011). Optically stimulated luminescence characteristics of modern flash-flood deposits in small mountain catchments. *Spectroscopy Letters*, *44*(7–8), 530–534. https://doi.org/10.1080/00387010.2011.610416
Middleton, T. A., Elliott, J. R., Rhodes, E. J., Sherlock, S., Walker, R. T., Wang, W., et al. (2017). Extension rates across the northern Shanxi Grabens, China, from Quaternary geology, seismicity, and geodesy. *Geophysical Journal International*, ggx031. https://doi.org/10.1093/gji/ggx031
Middleton, T. A., Walker, L. T., Parsons, B., Lei, Q., Zhou, Y., & Ren, Z. (2016). A major, intraplate, normal-faulting earthquake: The 1739 Yinchuan event in northern China. *Journal of Geophysical Research: Solid Earth*, *121*, 293–320. https://doi.org/10.1002/2015JB012355
Montgomery, D. R., & Foufoula-Georgiou, E. (1993). Channel network representation using digital elevation models. *Water Resources Research*, *29*, 1178–1191. https://doi.org/10.1029/93wr02463
Ntokos, D., Lykoudi, E., & Rondoyanni, T. (2016). Geomorphic analysis in areas of low-rate neotectonic deformation: South Epirus (Greece) as a case study. *Geomorphology*, *263*, 156–169. https://doi.org/10.1016/j.geomorph.2016.04.005
Perouse, E., Benedetti, L., Fleury, J., Rizza, M., Puliti, I., Billant, J., et al. (2018). Coseismic slip vectors of 24 August and 30 October 2016 earthquakes in central Italy: Oblique slip and regional kinematic implications. *Tectonics*, *37*, 3760–3781. https://doi.org/10.1029/2018tc005083
Pike, R. J., & Wilson, S. E. (1971). Elevation-relief ratio, hypsometric integral, and Geomorphic Area-Altitude Analysis. *The Geological Society of America Bulletin*, *82*, 1079–1084. https://doi.org/10.1130/0016-7606(1971)82[1079:erhiag]2.0.co;2
Proffett, J. M. (1977). Cenozoic geology of the Yerington district, Nevada, and implications for the nature and origin of Basin and Range faulting. *The Geological Society of America Bulletin*, *88*, 247–266. https://doi.org/10.1130/0016-7606(1977)88<247:cgotyd>2.0.co;2
Rao, G., He, C. Q., Chen, H. L., Yang, X., Shi, X., Chen, P., et al. (2020). Use of small unmanned aerial vehicle (sUAV)-acquired topography for identifying and characterizing active normal faults along the Seerteng Shan, North China. *Geomorphology*, *359*, 107168. https://doi.org/10.1016/j.geomorph.2020.107168
Rao, G., He, C. Q., Chen, P., Wu, Z., Hu, J., & Yao, Q. (2019). Active normal faulting along the Seerteng Shan, North China: Geometry and kinematics. *Journal of Asian Earth Sciences*, *184*, 103976. https://doi.org/10.1016/j.jseaes.2019.103976
Rao, G., Lin, A. M., Yan, B., Jia, D., & Wu, X. (2014). Tectonic activity and structural features of active intracontinental normal Faults in the Weihe Graben, central China. *Tectonophysics*, *636*(2014), 270–285. https://doi.org/10.1016/j.tecto.2014.08.019
Ren, Z. K., Zhang, Z. Q., Chen, T., Yan, S., Yin, J., Zhang, P., et al. (2016). Clustering of offsets on the Haiyuan fault and their relationship to paleoearthquakes. *GSA Bulletin*, B31155.1. https://doi.org/10.1130/B31155.1
Rimando, J., & Schoenbohm, L. M. (2020). Regional relative tectonic activity of structures in the Pampean flat slab segment of Argentina from 30 to 32°S. *Geomorphology*, *350*, 106908. https://doi.org/10.1016/j.geomorph.2019.106908
Rockwell, T. K., Keller, E. A., & Johnson, D. L. (1984). Tectonic geomorphology of alluvial fans and mountain fronts near Ventura, California. In M. Morisawa, & T. J. Hack (Eds.), *Tectonic Geomorphology* (pp. 183–207). Publication in Geomorphology, State University of New York.
Rood, D. H., Burbank, D. W., & Finkel, R. C. (2011). Spatiotemporal patterns of fault slip rates across the Central Sierra Nevada frontal fault zone. *Earth and Planetary Science Letters*, *301*, 457–468. https://doi.org/10.1016/j.epsl.2010.11.006
Schumm, S. A. (1956). Evolution of drainage systems and slopes in Badlands at Perth Amboy, New Jersey. *Bulletin of the Geological Society of America*, *67*, 597–646. https://doi.org/10.1130/0016-7606(1956)67[597:eodsas]2.0.co;2
Shen, X. H., & Wang, Y. P. (1994). A preliminary study of the active characteristics of the piedmont of the Taibaiwei Mountain. *North China Earthquake Sciences*, *12*(No.3), 17–26.
Shi, W., Cen, M., Chen, L., Wang, Y., Chen, X., Li, J., & Chen, P. (2015). Evolution of the late Cenozoic tectonic stress regime in the Shanxi Rift, central North China Plate inferred from new fault kinematic analysis. *Journal of Asian Earth Sciences*, *114*, 54–72. https://doi.org/10.1016/j.jseaes.2015.04.044
Silva, P. G., Goy, F. L., Zazo, C., & Bardají, T. (2003). Fault-generated mountain fronts in southeast Spain: Geomorphologic assessment of tectonic and seismic activity. *Geomorphology*, *50*, 203–225. https://doi.org/10.1016/s0169-555x(02)00215-5
State Seismological Bureau (SSB). (1988). *Research on active faults system around the Ordos block*. Seismological Press.
Strahler, A. N. (1952). Hypsometric (area-altitude) analysis of erosional topography. *Bulletin of the Geological Society of America*, *63*, 1117–1142. https://doi.org/10.1130/0016-7606(1952)63[1117:haaoet]2.0.co;2
Styron, R. (2019). The impact of earthquake cycle variability on neotectonic and paleoseismic slip rate estimates. *Solid Earth*, *10*, 15–25. https://doi.org/10.5194/se-10-15-2019
Sun, W. (2018). *Late Quaternary activity of Liuleng mountain north fault*. Institute of Geology, China Earthquake Administration.
Thompson, J. A., Chen, J., Yang, H., Li, T., Bookhagen, B., & Burbank, D. (2018). Coarse- versus fine-grain quartz OSL and cosmogenic ^{10}Be dating of deformed fluvial terraces on the northeast Pamir margin, northwest China. *Quaternary Geochronology*, *46*, 1–15. https://doi.org/10.1016/j.quageo.2018.01.002
Thompson, S. C., Weldon, R. J., Rubin, C. M., Abdrakhmatov, K., Molnar, P., & Berger, G. W. (2002). Late Quaternary slip rates across the central Tien Shan, Kyrgyzstan, Central Asia. *Journal of Geophysical Research*, *107*(B9), 2203. https://doi.org/10.1029/2001JB000596
Villamor, P., & Berryman, K. (2001). A late Quaternary extension rate in the Taupo Volcanic Zone, New Zealand, derived from fault slip data. *New Zealand Journal of Geology and Geophysics*, *44*, 243–269. https://doi.org/10.1080/00288306.2001.9514937
Walker, R. T., Bezmenov, Y., Begenjev, G., Carolin, S., Dodds, N., Gruetzner, C., et al. (2021). Slip-Rate on the main Köpetdag (Kopeh Dagh) strike-slip fault, Turkmenistan, and the active tectonics of the South Caspian. *Tectonics*, *40*. https://doi.org/10.1029/2021TC006846
Wan, Y. G., Shen, Z. K., Shang, D., Li, T. M., & Zeng, Y. H. (2006). Crustal stress evolution over the past years in North China and earthquake occurrence. *Earthquake Research in China*, *20*(No. 3), 244–261.
Wang, D., Chang, H., Yin, G. M., Han, F., Mao, Z., Du, J., et al. (2021). Spatial changes in late Quaternary slip rates along the Gyaring Co Fault: Implications for strain partitioning and deformation modes in Central Tibet. *Tectonics*, *40*. https://doi.org/10.1029/2020TC006110
Wang, L. (2012). *Research of basin marginal active normal faults through multi-scale tectonic geomorphology—A case study on the Yuguang Basin South Margin Fault*. Institute of Geology, China Earthquake Administration.

Wang, M., & Shen, Z. K. (2020). Present-day crustal deformation of continental China derived from GPS and its tectonic implications. *Journal of Geophysical Research: Solid Earth*, *125*, e2019JB018774. https://doi.org/10.1029/2019JB018774

Wei, Z. Y., He, H. L., Sun, W., Zhuang, Q., & Liang, Z. (2020). Investigating thrust-fault growth and segment linkage using displacement distribution analysis in the active Dushanzi thrust fault zone, Northern Tian Shan of China. *Journal of Structural Geology*, *113*, 103990. https://doi.org/10.1016/j.jsg.2020.103990

Wells, D. L., & Coppersmith, K. J. (1994). New empirical relationships among magnitude, rupture length, rupture width, rupture area, and surface displacement. *Bulletin of the Seismological Society of America*, *84*(4), 974–1002.

Westoby, M. J., Brasington, J., Glasser, N. F., Hambrey, M. J., & Reynolds, J. M. (2012). "Structure-from-Motion" photogrammetry: A low-cost, effective tool for geoscience applications. *Geomorphology*, *179*, 300–314. https://doi.org/10.1016/j.geomorph.2012.08.021

Whittaker, A. C., & Walker, A. S. (2015). Geomorphic constraints on fault throw rates and linkage times: Examples from the Northern Gulf of Evia, Greece. *Journal of Geophysical Research: Earth Surface*, *120*, 137–158. https://doi.org/10.1002/2014JF003318

Wilkinson, M. W., Jones, R. R., Woods, C. E., Gilment, S. R., McCaffrey, K. J. W., Kokkalas, S., & Long, J. J. (2016). A comparison of terrestrial laser scanning and structure-from motion photogrammetry as methods for digital outcrop acquisition. *Geosphere*, *12*, 1865–1880. https://doi.org/10.1130/GES01342.1

Wobus, C., Whipple, K. X., Kirby, E., Snyder, N., Johnson, J., Spyropolou, K., et al. (2006). Tectonics from topography: Procedures, promise, and pitfalls. In S. D. Willett, N. Hovius, M. T. Brandon, & D. M. Fisher (Eds.), *Tectonics, climate, and landscape evolution* (Vol. *398*, pp. 55–74). Geological Society of America Special Paper. https://doi.org/10.1130/2006.2398(04)

Wu, C. Y., Zheng, W. J., Zhang, P. Z., Zhang, Z., Jia, Q., Yu, J., et al. (2019). Oblique thrust of the Maidan fault and late Quaternary tectonic deformation in the southwestern Tian Shan, Northwestern China. *Tectonics*, *38*, 2625–2645. https://doi.org/10.1029/2018TC005248

Xiong, J. G., Li, Y. L., Zhong, Y. Z., Lu, H., Lei, J., Xin, W., et al. (2017). Latest Pleistocene to Holocene Thrusting Recorded by a Flight of Strath Terraces in the Eastern Qilian Shan, NE Tibetan Plateau. *Tectonics*, *36*, 2973–2986. https://doi.org/10.1002/2017TC004648

Xu, J., Song, C. Q., & Chu, Q. Z. (1998). Preliminary study on the seismotectonic characters of the Zhangjiakou-Penglai Fault Zone. *Seismology and Geology*, *20*(No.2), 146–154.

Xu, W., Liu, X. D., & Zhang, S. M. (2011). Late Quaternary faulted landforms and determination of slip rates of the middle part of Kouquan Fault. *Seismology and Geology*, *33*(2), 335–346.

Xu, X. W., Han, Z. J., Yang, X. P., Zhang, S., Yu, G., Zhou, B., et al. (2016). *Seismotectonic map of China and its adjacent regions*. Seismological Press.

Xu, X. W., & Ma, X. Y. (1992). Geodynamics of the Shanxi Rift system, China. *Tectonophysics*, *208*(1992), 325–340. https://doi.org/10.1016/0040-1951(92)90353-8

Xu, X. W., Ma, X. Y., & Deng, Q. D. (1993). Neotectonic activity along the Shanxi rift system, China. *Tectonophysics*, *219*, 305–325. https://doi.org/10.1016/0040-1951(93)90180-r

Xu, X. W., Wu, W. M., & Zhang, X. K. (2002). *New changing of crustal tectonic and earthquake in Capital Circle*. Science Press.

Xu, X. W., Wu, Y. X., Yu, G. H., Tan, X., & Li, K. (2017). Seismo-geological signatures for identifying M ≥ 7.0 earthquake risk areas and their preliminary application in mainland China. *Seismology and Geology*, *39*(2), 219–275.

Xu, X. W., Yonekura, N., Suzuki, Y., Noboyuki, Y., & Yasuhiro, S. (1996). Geomorphic study on late Quaternary irregular faulting along the Northern Piedmont of Liulengshan Range, Shanxi Province. *Seismology and Geology*, *18*(2), 169–181.

Xu, Y. R., He, H. L., Deng, Q. D., Allen, M. B., Sun, H., & Bi, L. (2018). The CE 1303 Hongdong earthquake and the Huoshan Piedmont Fault, Shanxi Graben: Implications for magnitude limits of normal fault earthquakes. *Journal of Geophysical Research: Solid Earth*, *123*. https://doi.org/10.1002/2017jb014928

Yıldırım, C. (2014). Relative tectonic activity assessment of the Tuz Gölü Fault Zone; Central Anatolia, Turkey. *Tectonophysics*, *630*, 183–192. https://doi.org/10.1016/j.tecto.2014.05.023

Zhang, H. Q., Huang, Q. H., Zhao, G. Z., Guo, Z., & Chen, Y. J. (2016). Three-dimensional conductivity model of crust and uppermost mantle at the northern Trans North China Orogen: Evidence for a mantle source of Datong volcanoes. *Earth and Planetary Science Letters*, *453*, 182–192. https://doi.org/10.1016/j.epsl.2016.08.025

Zhang, H. Y., Xie, F. R., & Jing, Z. J. (2009). Research on heterogeneity of the present tectonic stress field in the basin-and-range province northwest of Beijing. *Chinese Journal of Geophysics*, *52*(12), 3061–3071. https://doi.org/10.1002/cjg2.1382

Zhang, P. Z., Deng, Q. D., Zhang, G. M., Ma, J., Gan, W., Min, W., et al. (2003). Active crustal blocks and strong earthquakes in continental China. *Science in China (Series D)*, *33*, 12–20.

Zhang, Y. G., Zheng, W. J., Wang, Y. J., Zhang, D. L., Tian, Y. T., Wang, M., et al. (2018). Contemporary deformation of the North China Plain from Global Position System data. *Geophysical Research Letters*, *45*, 1851–1859. https://doi.org/10.1002/2017GL076599

Zhang, Y. Q., Ma, Y. S., Yang, N., Wei, S., & Shuwen, D. (2003). Cenozoic extensional stress evolution in North China. *Journal of Geodynamics*, *36*, 591–613. https://doi.org/10.1016/j.jog.2003.08.001

Zhang, Y. Q., Mercier, J. L., & Vergély, P. (1998). Extension in the graben systems around the Ordos (China), and its contribution to the extrusion tectonics of south China with respect to Gobi-Mongolia. *Tectonophysics*, *285*(1–2), 41–75. https://doi.org/10.1016/s0040-1951(97)00170-4

Zhao, B., Zhang, C. H., Wang, D. Z., Huang, Y., Tan, K., Du, R., & Liu, J. (2017). Contemporary kinematics of the Ordos block, North China and its adjacent rift systems constrained by dense GPS observations. *Journal of Asian Earth Sciences*, *135*, 257–267. https://doi.org/10.1016/j.jseaes.2016.12.045

Zhao, J. X. (2013). *OSL dating of sediments related to late Quaternary geomorphology of northern piedmont of the Hengshan Mountain*. Beijing: China University of Geosciences.

Zheng, X. Q., Li, Y. M., Chen, Z., Guilu, L., & Zhongyi, D. (2000). Majuanxiang underground thermal water system in Yanggao-Tianzhen Basin. *Journal of Taiyuan University of Technology*, *31*(1), 68–71.

Zhou, Y. L., You, H. C., Yang, J. L., Bian, Q., & Peng, Y. (2016). Geometrical characteristics and tectonic activities of Northern Margin Fault of the Huaian Basin. *North China Earthquake Sciences*, *34*(1), 47–52.

Zielke, O., Arrowsmith, J. R., Grant- Ludwig, L., & Akçiz, S. O. (2010). Slip in the 1857 and earlier large earthquakes along the Carrizo Plain, San Andreas Fault. *Science*, *327*, 1119–1122. https://doi.org/10.1126/science.1182781

Zuo, J. M., Wu, Z. H., Ha, G. H., Hu, M., Zhou, C., & Gai, H. (2021). Spatial variation of nearly NS-trending normal faulting in the southern Yadong-Gulu rift, Tibet: New constraints from the Chongba Yumtso fault, Duoqing Co graben. *Journal of Structural Geology*, *144*, 104256. https://doi.org/10.1016/j.jsg.2020.104256

References From the Supporting Information

Aitken, M. J. (1998). *Introduction to optical dating: The dating of quaternary sediments by the use of photon-stimulated luminescence*. Clarendon Press.

Chen, C. Y., He, J. M., Li, L. Y., & Du, L. (2016). Analysis of the deformation characteristics of Zhangjiakou-Bohai fault zone and its adjacent regions based on cross-fault observation data and GPS data. *South China Journal of Seismology*, *36*(No.3), 17–28.

Cheng, S. P., & Yang, G. Z. (1998). Fault growth, displacement transfer, and evolution of the Jiugongkou Fault overlap zone in Weixian, Hebei. *Seismology and Geology*, *20*(No.1), 1–8.

Ding, R., Ren, J. J., & Zhang, S. M. (2009). Late Quaternary activity and paleoearthquakes along the Nanyukou Segment of the Northern Piedmont Fault of the Wutai Mountain. *Earthquake Research in China*, *25*(No.1), 41–53.

Jiang, W. L., Xie, X. S., Wang, H. Z., Feng, X. Y., & Zhang, K. F. (2003). Holocene paleoseismic activities along the Northern Piedmont Fault of Hengshan Mountain, Datong Basin, Shanxi Province. *Earthquake Research in China*, *19*(No.1), 8–19.

Lu, Y. C., Wang, X. L., & Wintle, A. G. (2007). A new OSL chronology for dust accumulation in the last 130,000 a for the Chinese Loess Plateau. *Quaternary Research*, *67*(1), 152–160. https://doi.org/10.1016/j.yqres.2006.08.003

Murray, A. S., & Wintle, A. G. (2000). Luminescence dating of quartz using an improved single-aliquot regenerative-dose protocol. *Radiation Measurements*, *32*, 57–73. https://doi.org/10.1016/s1350-4487(99)00253-x

Murray, A. S., & Wintle, A. G. (2003). The single aliquot regenerative dose protocol: Potential for improvements in reliability. *Radiation Measurements*, *37*, 377–381. https://doi.org/10.1016/s1350-4487(03)00053-2

Prescott, J., & Hutton, J. (1994). Cosmic ray contributions to dose rates for luminescence and ESR dating: Large depths and long-term time variations. *Radiation Measurements*, *23*(2–3), 497–500. https://doi.org/10.1016/1350-4487(94)90086-8

Rees-Jones, J. (1995). Optical dating of young sediments using fine-grain quartz. *Ancient TL*, *13*(2), 9–14.

Zhou, Y. L., You, H. C., & Yang, Q. Y. (2018). Geometry and deformation transformation of the Ximalin Fault. *Seismology and Geology*, *40*(No.1), 57–70. https://doi.org/10.3969/j.issn.0253-4967.2018.01.005